JМ PAPERS

On the stability characteristics of a hypersonic boundary-layer flow over parametrised sinusoidal surface roughness

Bijaylakshmi Saikia[1] [ID] **and Christoph Brehm**[1]

[1]Department of Aerospace Engineering, University of Maryland, College Park, MD 20742, USA

Corresponding authors: Bijaylakshmi Saikia, bijaylakshmi.iitb@gmail.com; Christoph Brehm, cbrehm1@umd.edu

The stability characteristics of a Mach 5.35 boundary-layer flow over a flat plate with parametrised two-dimensional sinusoidal surface roughness are investigated. The investigation involves varying the roughness height from 10 % to 44 % of the boundary-layer thickness and exploring wavelengths ranging between 0.44 and 3.56 times the dominant second-mode wavelength in the region. The introduction of surface roughness leads to notable variations in the mean flow, resulting in separation behind the roughness elements and the propagation of local compression and expansion waves into the free stream. Stability investigations involved the utilisation of wave packet tracking in a linear disturbance simulation (LDS) framework and linear stability theory. The findings revealed significant effects on Mack modes including a reduction in frequency corresponding to maximum amplification with increased roughness height. Proper scaling of the dominant wavelength facilitates a collapse of the growth rate data. In contrast to the commonly reported stabilisation effects for roughness wavelengths significantly larger than the instability mode's wavelength, the findings primarily revealed destabilisation compared with the smooth-wall case, except for cases with very small roughness wavelengths and large amplitudes approaching the threshold of being classified as porous media. The LDS findings depicted lobed wall pressure amplitude plots, indicating potential undiscovered instability mechanisms or differences compared with the smooth wall. A detailed stability analysis elucidates these LDS findings, establishing a connection between the lobed amplitude structures and substantial changes in local stability characteristics, along with the emergence of Mack's first, second and third modes.

Key words: high-speed flow, boundary layer receptivity, boundary layer stability

---

1. Introduction

Thermal protection systems play a critical role in maintaining the structural integrity of hypersonic vehicles under extreme aerodynamic heating conditions during entry. Ablation, a key mechanism in thermal protection system functionality, involves coupled mass, momentum and energy transfer and can involve material removal. One intriguing phenomenon resulting from fluid–ablation interaction is the formation of cross-hatching patterns on certain sublimating or melting ablators promoting regular periodic surface features. Regular roughness patterns can also emerge in state-of-the-art ablators composed of woven composite materials, where the underlying structure is exposed during the ablation process. These surface features interact with the boundary layer, potentially generating acoustic-like disturbances, accelerating the transition to turbulence, and increasing heat transfer. In addition to the surface recession, outgassing is often accompanied by ablation, both of which can significantly influence the laminar-to-turbulent transition process, as discussed in Schneider (2008*b*, 2010). The phenomenon of ablation-induced roughness has been the subject of extensive research since the 1960s and 1970s. A review of existing experimental ground-based and flight studies on hypersonic boundary-layer transition can be found in Schneider (2008*a*).

Modelling arbitrary surface roughness is a challenging task. Spectral and fractal models to reproduce realistic roughness shapes can be employed to understand how the various roughness parameters affect boundary- layer transition, such as roughness shape, spacing, height, orientation and distribution, which is critical for understanding roughness effects. If the amplitude of the roughness is small, it is possible to treat each mode independently, with a single mode often sufficient to explain the flow modifications, as indicated by Floryan (1997). However, for larger roughness elements, even in the context of simplified two-dimensional patterns, our understanding remains limited, particularly regarding high-speed flows.

The influence of surface roughness on low-speed flows has been extensively documented in the literature (Loiseau *et al.* 2014; Bucci *et al.* 2018; Ma & Mahesh 2022; Zoppini *et al.* 2022). Additionally, the examination of discrete roughness elements and boundary-layer trips in high-speed flows has been the subject of numerous studies (Berry *et al.* 2001; Semper & Bowersox 2017; Shrestha & Candler 2019). However, there is a notable deficiency in research focusing on distributed thermal protection system roughness within the context of hypersonic flow. While certain existing studies have addressed distributed roughness in hypersonic settings, they predominantly investigated blunt entry capsule geometries, where the boundary layer is primarily subsonic, leading to fundamentally different flow characteristics (Braga *et al.* 2024*b*; Hollis 2021). Moreover, several high-speed flow studies, such as those conducted by Iyer *et al.* (2011, 2012), Muppidi & Mahesh (2012), Di Giovanni & Stemmer (2018, 2019) and Choudhari, Li & Paredes (2018), have explored roughness patches, typically characterised by regular shapes. However, these studies have primarily concentrated on the instability and breakdown mechanisms in the wake of the roughness features.

For roughness elements that are sufficiently large to induce notable mean-flow distortion, traditional stability approaches, including local linear stability theory (LST) and parabolised stability equations, may not provide accurate predictions when integrated across individual roughness features. In such cases, the application of harmonic linearised Navier–Stokes (HLNS) equations, as discussed in studies such as Zhao, Dong & Yang (2019), Haas *et al.* (2020) and Paredes *et al.* (2024), is essential to appropriately address the scattering effects present in strongly distorted mean flows. For example, Zhao *et al.* (2019) analysed two-dimensional humps and indentations, computing transmission coefficients

and revealing that the synchronisation frequency critically determines whether instability modes are suppressed or amplified. Similar stabilisation and destabilisation trends for discrete roughness placement relative to the synchronisation point have been observed in Fong, Wang & Zhong (2014). Further, Dong & Zhao (2021) developed an asymptotic triple-deck-based theory to examine the effects of isolated roughness elements, aligning closely with HLNS results even at roughness heights up to 25 % of the boundary-layer thickness. Their work highlighted the role of disturbance interactions with the main layer of the distorted flow field and the inhomogeneous forcing from the curved wall, which are the key contributors. Several other studies (e.g. Bountin *et al.* 2013; Zhou *et al.* 2017; Si *et al.* 2019) have demonstrated stabilisation of second-mode disturbances in high-frequency bands while amplifying lower-frequency perturbations for two-dimensional roughness with wavelengths significantly larger than the instability wavelengths.

A recent study by Braga *et al.* (2024*a*,*b*) investigated regular fully three-dimensional roughness patterns in a Mach 6 flow around a circular cylinder, successfully reproducing experimental findings by Hollis (2021). This study also demonstrated that the destabilisation effects in the predominantly subsonic boundary layer could be well predicted using two-dimensional stability analysis based on spanwise- and wavelength-averaged profiles. The findings suggest that the effects on primary instability mechanisms, particularly the destabilisation of the Tollmien–Schlichting mode, can be effectively elucidated through two-dimensional analysis. Similar results were obtained in Brehm *et al.* (2011) and Brehm & Fasel (2013) for an incompressible Blasius boundary-layer flow with two-dimensional distributed roughness patterns considering different roughness shapes, achieving close agreement with low-speed experimental data. Whilst these observations certainly do not translate into a general statement about destabilisation mechanisms of three-dimensional roughness patterns, they justify the value of performing stability investigation of two-dimensional roughness patterns and how they affect primary instability mechanisms even in three dimensions. In this work, we model wall roughness using regular sinusoidal patterns and conduct stability investigation by varying roughness amplitude and wavelength. The main objective of this work is to elucidate the physical mechanisms driving instability growth over these very regular surface roughness patterns. By isolating individual parameters, such as roughness length and height, we aim to deepen our understanding of their influence on transition processes in hypersonic boundary layers. Additionally, the potential emergence of new instability modes due to the presence of roughness is explored.

The organisation of the paper is as follows. The governing equations for the mean flow and small-amplitude disturbances are introduced in § 2. The test cases constructed to study the effects of roughness parameters are discussed in § 3. The effects of varying the roughness amplitude on the mean and the disturbance flow field are presented in § 4. Section 5 addresses the effects of a variation in the roughness wavelength. Finally, a summary of this work is provided in § 6.

2. Governing equations

The mean flow field is obtained by solving the compressible Navier–Stokes equations, which can be written as

$$\frac{\partial U}{\partial t} + \frac{\partial \mathbf{F_i}}{\partial x_i} + \frac{\partial \boldsymbol{F}_{v_i}}{\partial x_i} = \mathbf{0}, \tag{2.1}$$

where

$$U = \begin{bmatrix} \rho \\ \rho u \\ \rho v \\ E \end{bmatrix}; \quad F = \begin{bmatrix} \rho u_i \\ \rho u u_i + P\delta_{1i} \\ \rho v u_i + P\delta_{2i} \\ (E + P)u_i \end{bmatrix}; \quad F_v = \begin{bmatrix} 0 \\ -\tau_{1i} \\ -\tau_{2i} \\ -\kappa \frac{\partial T}{\partial x_i} - \tau_{ij}u_j \end{bmatrix}. \quad (2.2)$$

Here, U is the solution vector of the conservative variables and F and F_v are the inviscid and viscous fluxes, respectively. The first component of the vector equation in (2.1) corresponds to the continuity equation. The following two components correspond to the momentum equations in the x and y directions, respectively. Parameters u, v, P and τ_{ij} are the x and y velocity, thermodynamic pressure and stress tensor components. The total energy equation is listed in the last component of (2.1) where E consists of internal energy and the kinetic energy of the gas. Fourier's law of heat conduction is used to evaluate the heat flux vector. Viscosity is determined in accordance with Sutherland's law, while the thermal conductivity κ has been calculated using a Prandtl number of 0.72. The specific heat ratio is considered as 1.4, given that the working fluid is air.

To derive the equations governing the small-amplitude disturbances, we recast the conservative form of the Navier–Stokes equations (2.1) into a primitive variable form by using a conservative to primitive transformation matrix ($\partial \tilde{U} / \partial \tilde{Q}$). The instantaneous state vector of the primitive variables $Q = [P, u, v, T]^T$ is decomposed into a steady mean flow $\bar{Q}$ and an unsteady disturbance flow field $\tilde{Q}$. Since the mean flow satisfies the Navier–Stokes equations, it is subtracted from the instantaneous state vector Q to obtain the governing equations for the disturbances. After neglecting the nonlinear terms in the disturbances, the governing equation for the disturbance flow can be written as

$$\frac{\partial \tilde{U}}{\partial \tilde{Q}} \frac{\partial \tilde{Q}}{\partial t} + \frac{\partial \tilde{F}_i}{\partial x_i} + \frac{\partial \tilde{F}_{v_i}}{\partial x_i} = 0, \quad (2.3)$$

$$\tilde{U} = \begin{bmatrix} \tilde{\rho} \\ \tilde{\rho}\bar{u} + \bar{\rho}\tilde{u} \\ \tilde{\rho}\bar{v} + \bar{\rho}\tilde{v} \\ \tilde{E} \end{bmatrix}, \quad \tilde{F} = \begin{bmatrix} \tilde{\rho}\bar{u} + \bar{\rho}\tilde{u} \\ \bar{\rho}\bar{u}\tilde{u}_i + \bar{\rho}\bar{u}_i\tilde{u} + \tilde{\rho}\bar{u}\bar{u}_i + \tilde{P}\delta_{1i} \\ \bar{\rho}\bar{v}\tilde{u}_i + \bar{\rho}\bar{u}_i\tilde{v} + \tilde{\rho}\bar{v}\bar{u}_i + \tilde{P}\delta_{2i} \\ (\bar{E} + \bar{P})\tilde{u}_i + (\tilde{E} + \tilde{P})\bar{u}_i \end{bmatrix} \quad \text{and} \quad (2.4)$$

$$\tilde{F}_v = \begin{bmatrix} 0 \\ -\tilde{\tau}_{1i} \\ -\tilde{\tau}_{2i} \\ -\tilde{\kappa}\frac{\partial \bar{T}}{\partial x_i} - \bar{\kappa}\frac{\partial \tilde{T}}{\partial x_i} - \tilde{\tau}_{ij}\bar{u}_j - \bar{\tau}_{ij}\tilde{u}_j \end{bmatrix}. \quad (2.5)$$

The primitive state vector used here to represent the disturbance flow is $\tilde{Q} = [\tilde{p}, \tilde{u}, \tilde{v}, \tilde{T}]^T$, where the tilde denotes the disturbance flow quantities and the overbar is used for the mean flow. The total energy of the disturbance can be written as $\tilde{E} = \bar{\rho}C_v\tilde{T} + \tilde{\rho}C_v\bar{T} + \bar{\rho}\bar{u}\tilde{u} + \bar{\rho}\bar{v}\tilde{v} + 0.5\tilde{\rho}(\bar{u}^2 + \bar{v}^2)$. The specific heat and the specific gas constant are represented by C_v and R, respectively. Disturbance flow simulations are performed by solving the linear disturbance equations with the wave packet simulation approach using the same curvilinear mesh used for computing the mean flow. Adaptive mesh refinement (AMR) in an immersed boundary framework (AMR-IBM-WPT) is also employed to efficiently track wave packets as detailed in Browne *et al.* (2019, 2020).

3. Simulation set-up

The simulation set-up to study the parametric variation of surface roughness is designed based on the boundary-layer thickness and the wavelength of the second mode computed at the end of an $L = 1$ m long smooth flat plate.

To obtain these two values, we first computed a two-dimensional Mach 5.35 flow over a smooth flat plate at a free-stream temperature of 64.316 K and a unit Reynolds number of 14.356×10^6 m^{-1} by solving the compressible Navier–Stokes equations (2.1). The selection of this condition was based on its correspondence with the boundary-layer edge values of the 7° sharp cone examined in the Boeing/AFOSR Mach 6 quiet-flow Ludwieg Tube at Purdue University (after applying the Mangler transformation). This case has been extensively utilised in several other research studies to analyse the physical mechanisms leading to laminar-to-turbulent transition (Sivasubramanian & Fasel 2011; Haas *et al.* 2020; Browne *et al.* 2022).

The convective fluxes are calculated using a blended fifth-order weighted essentially non-oscillatory scheme as in Brehm *et al.* (2015), with Rusanov flux vector splitting, and the viscous fluxes are computed using a second-order centred finite-difference method. A first-order backward-difference scheme advances the mean-flow governing equations in pseudo-time until a steady state is reached. A self-similarity boundary-layer profile is prescribed at the inflow boundary at $x = 0.01$ m, and no-slip and adiabatic boundary conditions are applied at the wall. Leading-edge receptivity has been observed to play a pivotal role in the transition of high-speed boundary-layer flows influenced by environmental disturbances. Our prior research (Saikia & Brehm 2022) demonstrated the introduction of acoustic, vorticity and entropy waves ahead of the leading-edge shock wave while examining receptivity mechanisms for both smooth and rough surfaces under identical conditions. The primary focus of this paper does not encompass a receptivity study; therefore, the leading edge has been omitted. An extrapolation boundary condition is used at the computational domain's outflow and top boundary.

To introduce the two-dimensional sinusoidal roughness at the surface of the smooth, flat plate, the following analytical expression is used:

$$y_{rough} = y_{smooth} + 0.25 \max(A - y_{smooth}, 0) \cos\left(\frac{2\pi(x - x_s)}{\lambda}\right) - 0.25A, \qquad (3.1)$$

where y_{rough} and y_{smooth} denote the wall-normal distance for the flat plate with and without roughness, respectively. The roughness elements begin at $x_s = 0.026$ m and end at 0.978 m, whereas the computational domain spans $x = [0.01, 1]$ m. The top boundary is located at $y = 0.26$ m, and the lower boundary is a function of the roughness height. After a thorough grid convergence study, the streamwise and the wall-normal directions are discretised with 8000 and 500 grid points, respectively. Grid points are uniform in the streamwise direction, whereas in the wall-normal direction, points are clustered near the wall, with a minimum wall-normal spacing of $\Delta y_w = 5 \times 10^{-6}$ m.

The mean-flow velocity and temperature profiles along the wall-normal direction are plotted in figure 1(*a*) at $x = 1$ m. The dashed-dotted line in the figure denotes the boundary-layer thickness around $\delta_{0.99} = 4.6$ mm. The four test cases listed in table 1 are designed by varying the roughness amplitude from 10.4 % to 43.5 % of the boundary-layer height at $x = 1$ m with a fixed roughness wavelength of $\lambda = 8$ mm. The choice of the roughness wavelength is determined by the second-mode wavelength corresponding to the smooth flat plate, and this is elaborated upon in more detail in the following paragraphs.

To determine a suitable roughness wavelength based on the dominant instability mechanisms, we computed the disturbance flow field over the smooth flat plate by solving
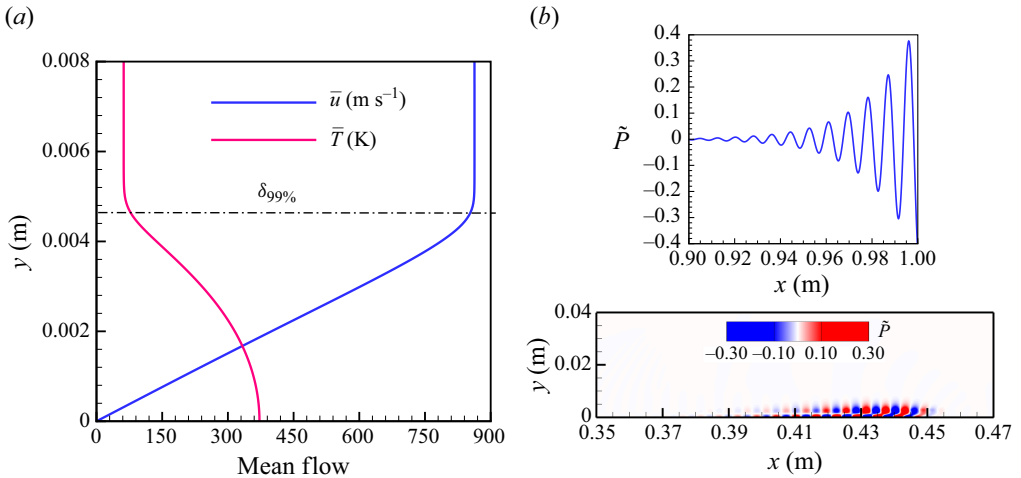
Figure 1. (*a*) Variation of the streamwise velocity and temperature along the wall-normal direction extracted at $x = 1$ m for the smooth flat plate, with the black dashed-dotted line indicating the boundary-layer thickness. (*b*) A line plot of disturbance wall pressure and contours visualising the second-mode-dominated packet are shown in the top and bottom panels for the smooth flat plate at Mach 5.35.

Case	Amplitude, A (mm)	$A/A_{x=1m}$ (%)	Wavelength, λ (mm)
W2A1	0.48	10.4	8
W2A2	0.96	20.9	8
W2A3	1.5	32.6	8
W2A4	2	43.5	8

Table 1. Test cases constructed to study the effects of varying roughness height with a fixed wavelength of 88.9 % of the second-mode wavelength.

the linear disturbance equation (2.3). Time integration has been carried out using a second-order Runge–Kutta scheme. Like the mean flow field, an extrapolation boundary condition is applied at the outflow and top boundary. At the inlet, Dirichlet boundary conditions are imposed on the primitive variables. Isothermal and no-slip conditions are applied at the wall, except at the forcing location, which spans $x = [0.02-0.026]$ m in the steamwise direction. A broadband pulse with a central frequency of $F = 100$ kHz is introduced into the flow field through the forcing slot to induce the formation of a wave packet dominated by the second mode. The forcing term is composed of a spatial and a temporal variation, which can be expressed as

$$G(x, t) = \begin{cases} A\cos^3(\pi x_h)\sin\left(-\frac{2\pi t}{T_f}\right) & \text{for } t \leqslant T_f \text{ and} \\ 0 & \text{for } t > T_f, \end{cases} \tag{3.2}$$

with $x_h = (x - 0.5(x_s + x_e))/(x_e - x_s)$.

Here, x_s and x_e represent the start and end location of the pulse in the streamwise direction. The amplitude of the pulse is denoted by A, T_f is the disturbance period and t denotes the time.

A snapshot of the instantaneous disturbance pressure field over the smooth flat plate is presented in figure 1(*b*), with the red and blue contours denoting the positive and

Case	Wavelength, λ (mm)	λ/λ_{2nd}	Amplitude, A (mm)
W1A2	4	0.44	0.96
W2A2	8	0.89	0.96
W3A2	16	1.78	0.96
W4A2	32	3.56	0.96

Table 2. Test cases constructed to study the effects of varying roughness wavelength with a fixed amplitude of 20.9 % of the smooth-wall boundary-layer thickness at $x = 1$ m.

negative values, respectively. The pulse with a forcing frequency of 100 kHz excites the second-mode instability waves in the flow, which can be identified from its typical two-cell structure near the wall. The variation of disturbance wall pressure close to the end of the computational domain is shown in the top panel of figure 1(*b*). It can be inferred that the second mode attains a wavelength of around $\lambda = 9$ mm at the end of the smooth flat plate. The test cases presented in table 1 are designed to have a fixed wavelength of 89 % of the second-mode wavelength. To study the effect of a change in the roughness wavelength, we constructed four test cases in table 2, where the wavelength of the distributed roughness is varied as a function of the second-mode wavelength ($= 9$ mm), keeping the roughness height fixed at 20.9 % of the boundary-layer thickness ($\delta_{0.99} = 4.6$ mm) at $x = 1$ m corresponding to the smooth flat plate.

4. Effect of roughness height

In the case of hypersonic flows, it was reported that very large roughness heights are required to affect the transition process (Schneider 2008*a*). Duan, Wang & Zhong (2010) showed that an isolated roughness element with a height equal to half of the boundary-layer thickness might delay the transition process. In this section, we vary the roughness height from 10.4 % to 43.5 % of the boundary-layer thickness and study its effect on the mean and the disturbance flow field. As the boundary layer grows along the plate, the ratio of the local boundary-layer thickness to the roughness height will increase monotonically since the roughness height is kept constant throughout the domain.

4.1. *Mean flow field*

The steady mean flow fields corresponding to the amplitude-varying cases from table 1 are shown in figure 2 in terms of instantaneous pressure contours. As the flow field will be qualitatively similar downstream, too, only the first four roughness elements are shown here. When the supersonic flow reaches the first roughness element at $x = 0.026$ m, an expansion fan is formed, followed by a compression wave. Across the expansion fan, the flow accelerates while reducing the temperature and the static pressure. The variation of pressure extracted at $y = 0$ is shown in figure 2(*e*) for the first two roughness elements. Moving across a single roughness element, the pressure and the temperature slowly increase over the converging area, which can be identified from a change of the contour colour from black to white in figure 2. As the roughness height is increased, the strength of the compression wave becomes slightly greater, which can be seen from a small increase in the peak value of non-dimensional pressure at $x = 0.033$ m in figure 2(*e*). The rough-wall case W2A4, which has the largest roughness height, leads to the maximum peak pressure.

The presence of the roughness also leads to flow recirculation, which is shown in terms of blue streamlines in figure 3. The separation region extends throughout the roughness element, which is typically classified as the d-type roughness. The red contours in figure 3
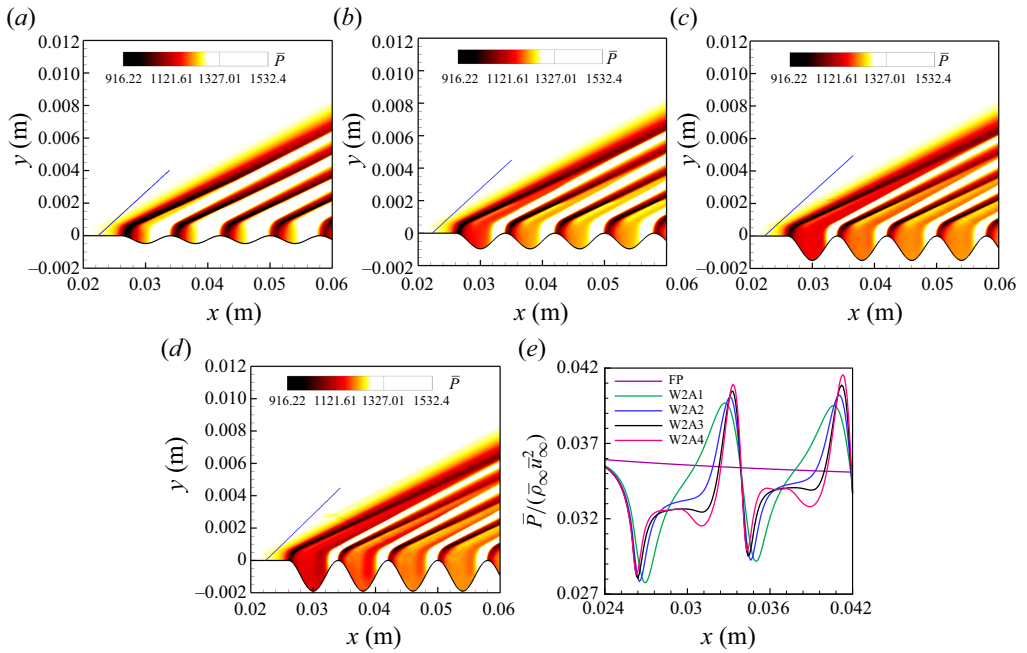
Figure 2. Contours of instantaneous pressure showing the effects of varying roughness height on the mean flow field for the rough-wall cases (*a*) W2A1, (*b*) W2A2, (*c*) W2A3 and (*d*) W2A4. The blue line indicates the Mach angle for each case. (*e*) The non-dimensional pressure for different cases is compared after extracting at $y = 0$.
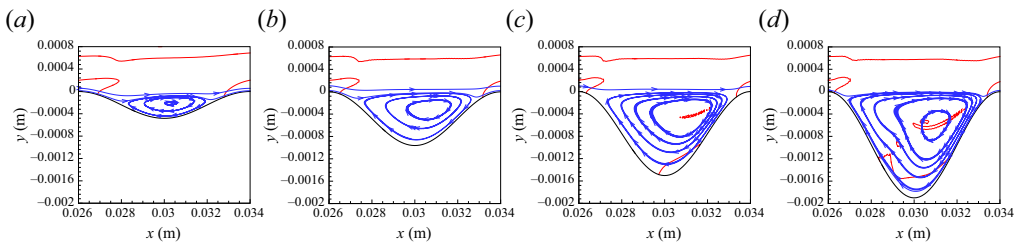

Figure 3. Region of flow circulation inside the roughness element centred at $x = 0.03$ m visualised in terms of blue streamlines for (*a*) W2A1, (*b*) W2A2, (*c*) W2A3 and (*d*) W2A4. The background red contours correspond to zero inflectional profiles.

represent the zero contours of $(\partial/\partial y)(\bar{\rho}(\partial\bar{u}/\partial y))$, indicating the presence of generalised inflection points (GIPs). The location of the GIP on top of the recirculation bubble does not seem to be affected by a change in the roughness height. However, additional GIPs are created inside the cavities for the larger-amplitude cases (see figures 3*c* and 3*d*).

A comparison of the boundary-layer profiles between the smooth- and rough-wall cases is presented in figure 4 after normalising by the corresponding free-stream value. For the smooth flat plate, the data are extracted at $x = 0.4$ m, whereas the profiles for the rough-wall cases are obtained along the grid lines in the wall-normal direction. This is indicated by the black lines in figure 4(*a*) for a roughness wavelength spanning $x = 0.3960$–0.4040 m. Subsequently, an averaging process was conducted along the grid lines parallel to the wall, which resulted in the averaged velocity and temperature profiles presented in figures 4(*b*) and 4(*c*), respectively. The boundary-layer profiles extracted across the roughness element are shifted upwards by adding the local roughness height
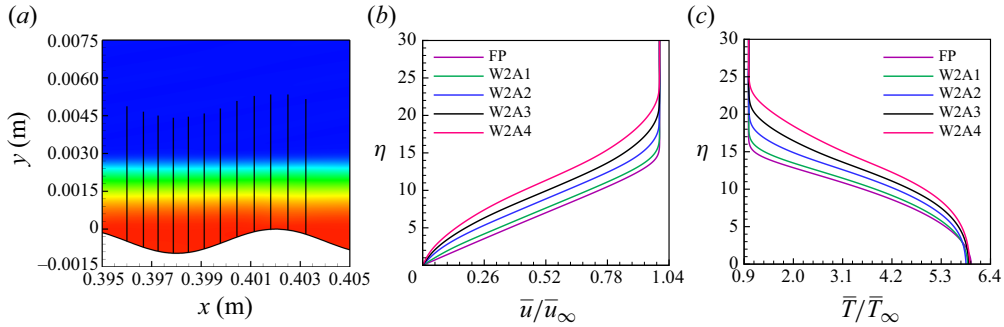
(a)

(b)

(c)

Figure 4. Comparison of (*b*) velocity and (*c*) temperature profiles averaged over a roughness wavelength for the amplitude-varying cases compared with the smooth-wall data extracted at $x = 0.4$ m. For the rough-wall cases, data are extracted along the vertical lines shown in (*a*) with background contours of mean-flow temperature.

such that the averaged profiles start from $y = 0$, similar to the smooth-wall case. The vertical coordinate η is the ratio of wall-normal distance y to the viscous length scale $H = (\mu_\infty x / \rho_\infty U_\infty)^{0.5}$. The Blasius length scale at $x = 0.4$ m is computed based on free-stream velocity U_∞, density ρ_∞ and dynamic viscosity μ_∞. The increase in roughness height results in a corresponding enhancement in the thickness of both the momentum and thermal boundary layers. Moreover, a rise in temperature within the boundary layer is observed as the roughness height is progressively increased. This alteration may affect the size of the relative supersonic region.

4.2. *Disturbance flow field*

Using the steady mean flow presented in the previous subsection, the disturbance flow field is computed by solving the linear disturbance equation (2.3) for the amplitude-varying cases. Snapshots of the disturbance pressure field are shown in figure 5. In contrast to the smooth flat plate, where pressure contours are predominantly observed in proximity to the wall, the rough-wall scenarios exhibit contours that extend further away from the surface, leading to a gradual decay of disturbances. This is due to the interaction between the wave packet and the supersonic wave patterns of the base flow, which are generated by the roughness elements, as depicted in figure 5(*a*). As the height of the surface roughness increases, the interaction between the disturbances occurring near the wall and the mean-flow pressure field becomes more pronounced (see figure 5*d*). Structures that resemble the second mode have been observed in proximity to the wall in the amplitude-varying cases. In comparison with the smooth wall, all rough-wall cases exhibit elevated pressure values. The rough-wall case W2A4, featuring the greatest roughness height, results in a slight decrease in disturbance pressure in comparison with the W2A3 case.

To conduct a comprehensive analysis of the disturbance field, a fast Fourier transform (FFT) of the wall-pressure signal was conducted in the time domain. The resulting logarithmic amplitude distribution is illustrated in figure 6, displayed as a function of streamwise location and frequency. For the rough-wall cases, the amplitude plots are shown after taking an average over each roughness wavelength throughout the domain (see figure 27 in Appendix A). A comparative analysis of the smallest-height case, W2A1, as illustrated in figure 6(*b*), with the smooth flat plate shown in figure 6(*a*) indicates that the introduction of distributed roughness, measuring just 10.4 % of the boundary-layer thickness, has a negligible effect on the amplitude loop. The amplitude loop identifies a region characterised by a significant increase in the Fourier-transformed wall-pressure
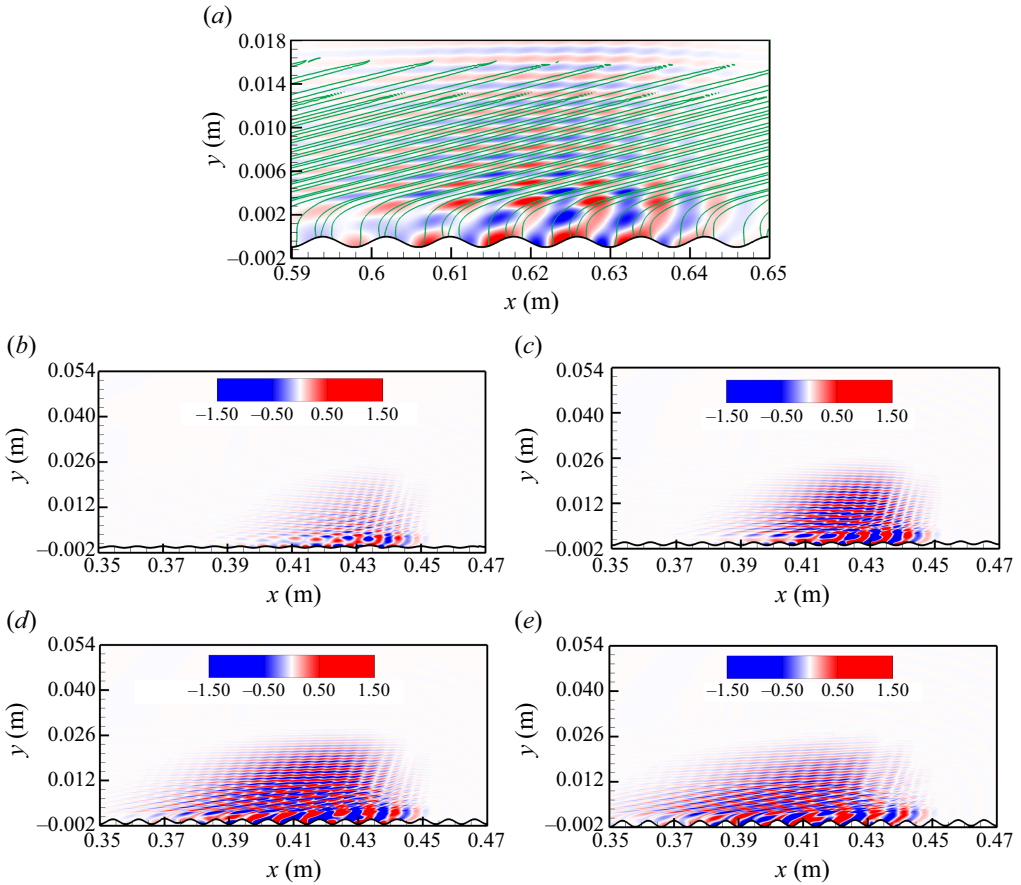
(*a*)

(*b*)

(*c*)

(*d*)

(*e*)

Figure 5. (*a*) The instantaneous mean-flow pressure field is delineated by green lines, accompanied by a background contour representing the disturbance pressure for the W2A2 case. Disturbance pressure field for the amplitude-varying cases (*b*) W2A1, (*c*) W2A2, (*d*) W2A3 and (*e*) W2A4.

amplitude, which points to potential areas of instability within the flow. An additional increase in the roughness height to 20.9 %, corresponding to the rough-wall case W2A2, results in an expansion of the high-amplitude region, as indicated by the red contours (see figure 6*c*). As the roughness height increases, the amplitude loop becomes larger and extends to lower disturbance frequencies. This is more evident for the larger-roughness cases W2A3 and W2A4 in figures 6(*d*) and 6(*e*), respectively. In these instances, the amplitude contours begin to delineate into two distinct regions. This may suggest that large roughness heights might lead to additional instability modes or even a previously undiscovered instability mechanism.

To identify the frequency range leading to the instability growth, the amplification rate ($-\alpha_i = \partial/\partial x \, (\log \, |\tilde{P}_w|)$) was computed based on the Fourier-transformed disturbance wall-pressure amplitude $|\tilde{P}_w|$. The growth rate for the smooth-wall case is extracted at $x = 0.4$ m, and for the rough-wall cases, it is computed based on the wall-pressure amplitude averaged over the roughness element spanning between $x = 0.396$ m and 0.404 m. The growth rate is plotted as a function of frequency in figure 7(*a*), and the black dashed line separates the unstable ($-\alpha_i > 0$) from the stable region. For the smooth-wall case, the second mode is the dominant instability, and the maximum amplification of this mode is observed at 116 kHz.
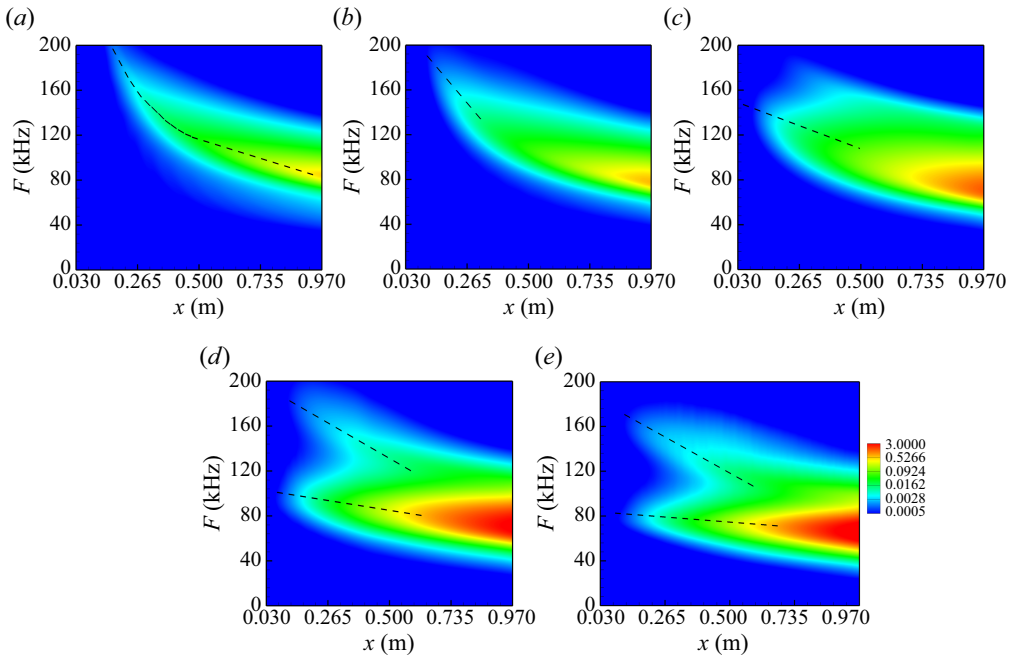
Figure 6. Logarithmic contours of disturbance pressure amplitude are illustrated as a function of frequency and streamwise location for the (*a*) smooth flat plate and amplitude-varying cases (*b*) W2A1, (*c*) W2A2, (*d*) W2A3 and (*e*) W2A4.

The presence of roughness reduces the growth rate of this mode at $x = 0.4$ m, and there is also a shift in the instability peak to a lower-frequency range. Including roughness elements at the wall increases the effective boundary-layer height (see figure 4), reducing the disturbance frequency corresponding to the peak growth rate.

Another instability mode at higher frequencies appears, which becomes unstable for roughness heights greater than or equal to 20.9 % of the boundary-layer thickness. Unlike the first peak, the second peak that appears at 152 kHz for the W2A2 case shows an increase in the amplification rate as the roughness height increases. It also moves to a lower-frequency range with increasing roughness height similar to the first peak in growth rate. Although not unstable, an additional peak is observed at 172 kHz for the largest-height case W2A4. A detailed discussion on identifying instability modes associated with these growth rate peaks is presented in § 4.3.

Figure 7(*b*) compares the amplification rates along the wall at frequencies corresponding to the peak growth rate of the first instability peak obtained from figure 7(*a*). Although the smooth-wall case shows the largest amplification at 116 kHz for $x = 0.4$ m, the growth rate of the second mode drops significantly after attaining the maximum growth and becomes stable after $x = 0.54$ m. The smallest-roughness case W2A1 also shows a similar trend and becomes stable slightly downstream ($x = 0.68$ m) of the smooth-wall location. The influence of roughness height is distinctly evident in the remaining three amplitude-varying cases, where the unstable region extends throughout the entire domain. This leads to increased disturbance pressure amplitudes observed at the end of the computational domain, as illustrated in figure 6. Notably, the case with the highest roughness height, designated as W2A4, results in the largest growth of instability at $x = 0.4$ m at a considerably lower frequency of 63 kHz, as demonstrated in figure 7(*b*).

Next, we computed the *N*-factor ($N = \log(A/A_o)$) curves for a range of frequencies with increments of $\Delta F = 2$ kHz to gain an idea about the transition onset location.
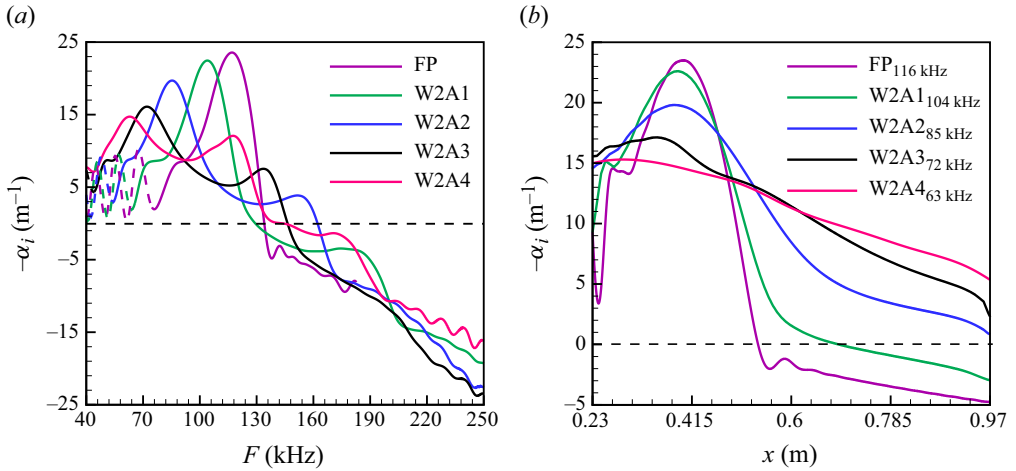
Figure 7. (*a*) Comparison of the averaged growth rate over a roughness wavelength centred at $x = 0.4$ m for the amplitude-varying cases compared with the smooth-wall data at varying frequencies. (*b*) Variation of the growth rate along the wall.
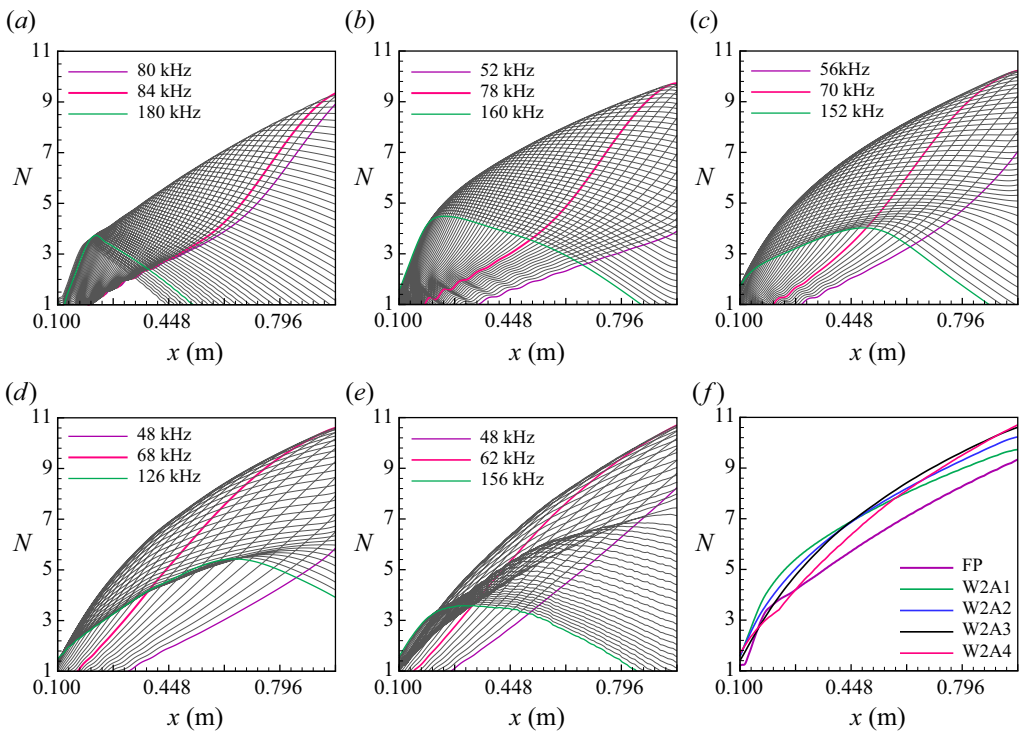

Figure 8. Effect of variation of roughness height on the N-factor for a range of disturbance frequency plotted along the wall with a frequency step of 2 kHz corresponding to the (*a*) smooth flat plate and amplitude-varying cases (*b*) W2A1, (*c*) W2A2, (*d*) W2A3 and (*e*) W2A4. The magenta line indicates the frequency leading to the maximum N-factor at the end of the domain. (*f*) The envelope of the maximum N-factor along the wall.

The purple and green lines in figure 31 denote the lowest and the highest frequencies, respectively, for each case. The magenta line in figure 8(*a–e*) corresponds to the frequency leading to the maximum *N*-factor at the end of the computational domain. A modest increase in the maximum *N*-factor has been observed, rising from 9.34 in the smooth-wall scenario to 9.72 for the small-roughness-height case designated as W2A1. This change is accompanied by a corresponding decrease in the frequency associated with the maximum *N*-factor, which declines from 84 kHz in the smooth-wall condition to 78 kHz in the rough-wall case. Increasing the roughness height to 20.9 % of the boundary-layer thickness increases the maximum *N*-factor to 10.2 for the W2A2 case at 70 kHz. Larger-roughness cases W2A3 and W2A4 attain the maximum *N*-factor of 10.6 and 10.7, respectively, at a much lower frequency of 68 and 62 kHz.

The variation of the *N*-factor envelope for each case is presented in figure 8(*f*). It can be observed that smaller-roughness cases show the largest increase in the *N*-factor envelope until approximately half of the computational domain ($x = 0.45$ m), where it approaches a value of around 7. However, towards the end of the domain, cases with larger roughness heights, specifically W2A3 and W2A4, yield the highest *N*-factor envelope values.

Therefore, adding distributed roughness of a small height, around 10.4 % of the boundary-layer thickness, can also increase the *N*-factor compared with a smooth-wall case.

Also, compared with a smooth flat plate, a surface consisting of larger roughness elements will lead to disturbance amplification at much lower frequencies (see figure 8*d*,*e*) due to an increase in the effective boundary-layer height. While the transition onset *N*-factor in free flight can reach approximately 14 (Borg *et al.* 2025), the smooth-wall case in this study achieves a peak value of only 9.34. Consequently, we have selected an *N*-factor of 8 for comparative analysis between the various cases presented in figure 28 in Appendix A. As the transition from laminar to turbulent flow is inherently three-dimensional in nature, the current investigations cannot be used to provide a precise transition location. Therefore, the primary objective of this two-dimensional study is not to accurately determine the location of transition onset. Rather, our aim is to comprehend the differences in the instability mechanisms between a smooth wall and a two-dimensional roughened wall. While the second mode is recognised as the dominant instability for the smooth flat plate, the introduction of distributed roughness results in the emergence of additional instability peaks as illustrated in figure 7(*a*). In the following section, we conduct a linear stability analysis to identify the instability modes associated with these observed growth rate peaks.

4.3. *Linear stability analysis for the amplitude-varying cases*

This section investigates the stability characteristics of the amplitude-varying cases using the linear stability solver presented in Tumin (2006, 2007). The stability solver is based on the linearised Navier–Stokes equations derived using the parallel flow assumption, which implies that the wall-normal velocity and the gradients of the mean flow in the streamwise direction are neglected. The global solver computes the full eigenspectrum using the single-domain Chebyshev spectral collocation method. Using the initial guess provided by the global solver, a more accurate prediction of the eigenvalue is obtained by utilising the local solver. The disturbance variables can be expressed using a normal-mode ansatz as $\boldsymbol{q}'(x, y, z, t) = \hat{\boldsymbol{q}}(y) \exp[i(\alpha x + \beta z - \omega t)]$, where $\boldsymbol{q}'$ denotes the instantaneous disturbance quantity and $\hat{\boldsymbol{q}}$ is the vector of eigenfunctions. For the spatial stability analysis conducted here, the streamwise wavenumber $\alpha = \alpha_r + i\alpha_i$ is complex, where $-\alpha_i$ represents the spatial growth rate. Using the real component of the wavenumber α_r and the

circular frequency ω, the non-dimensional phase speed for a two-dimensional disturbance (i.e. spanwise wavenumber $\beta = 0$) is computed as $c_r = \omega/\alpha_r$.

This LST solver was employed to investigate the influence of non-parallel flow on perturbations induced by roughness in low-speed boundary layers (Tumin 2008). The results revealed that although the outcomes incorporating non-parallel flow exhibited quantitative discrepancies compared with those obtained using the parallel flow approximation, the fundamental flow-field structure downstream of the roughness element remained consistent.

Since the linear stability analysis employs the parallel flow assumption, the results must be interpreted carefully as the flow past distributed roughness is highly non-parallel, especially at larger roughness heights. It is important to emphasise that the primary objective of utilising the LST solver was not to capture the amplification rates predicted by the linear disturbance simulation (LDS) precisely but rather to analyse the flow field with the aim of discerning the nature of instability modes present in the flow by examining the corresponding eigenfunctions. This tool is solely utilised to interpret the LDS results in the paper. Any discrepancy between the LST data and the LDS results serves to indicate the extent of non-parallelism in the flow.

4.3.1. *Stability analysis of the W2A2 case*

For the linear stability analysis, the roughness element centred around $x = 0.4$ m is considered corresponding to the rough-wall case W2A2. The mean-flow profiles are extracted along the vertical lines shown in figure 9(*a,d,g,j*). The streamwise velocity profiles along the wall-normal direction are plotted in figure 9(*b,e,h,k*). Although velocity profiles do not differ much away from the wall, the pressure profiles are significantly different due to the presence of compression and expansion waves generated by the rough surface. The insets in figure 9 emphasise the differing degrees of flow separation at various streamwise locations across the roughness element. Furthermore, the effective boundary-layer thickness varies along the roughness element due to changes in the local roughness height, with the maximum thickness observed at the trough of the roughness.

The linear stability solver indicates that the flow exhibits instability above the black dashed line, characterised by $-\alpha_i > 0$, as presented in figure 9(*c,f,i,l*). Notably, four distinct instability peaks are identified in figure 9(*c*), labelled as I, II, III and IV throughout the examined frequency range. The dominant instability peak II is observed within the frequency range of $54-140$ kHz. Meanwhile, instability peak I arises in the low-frequency range (<73 kHz) and remains unstable across all locations depicted in figure 9(*c*). In contrast, instability peak III is only unstable at the final three locations, while peak IV is completely stable.

As the roughness height transitions from $x = 0.3960$ to 0.3980 m, there is a notable shift in the frequency associated with the peak growth rates of all instability modes towards lower values. It is also observed that, unlike the first instability peak, the second and third peaks demonstrate increased amplification as the effective boundary-layer thickness grows from the first to the last x location.

Moving up the roughness element (figure 9*d,g*), the effective boundary-layer height reduces, as can be seen from the variation of the streamwise velocity profiles in figure 9(*e,h*). Notably, the instability peaks identified in figure 9(*f,i*) shift to a higher-frequency range, accompanied by a decrease in their growth rate. This behaviour contrasts with the findings presented in figure 9(*c*). Additionally, the third instability peak in figure 9(*i*) spans a broader frequency range ($197-355$ kHz) compared with the peak observed in figure 9(*f*).
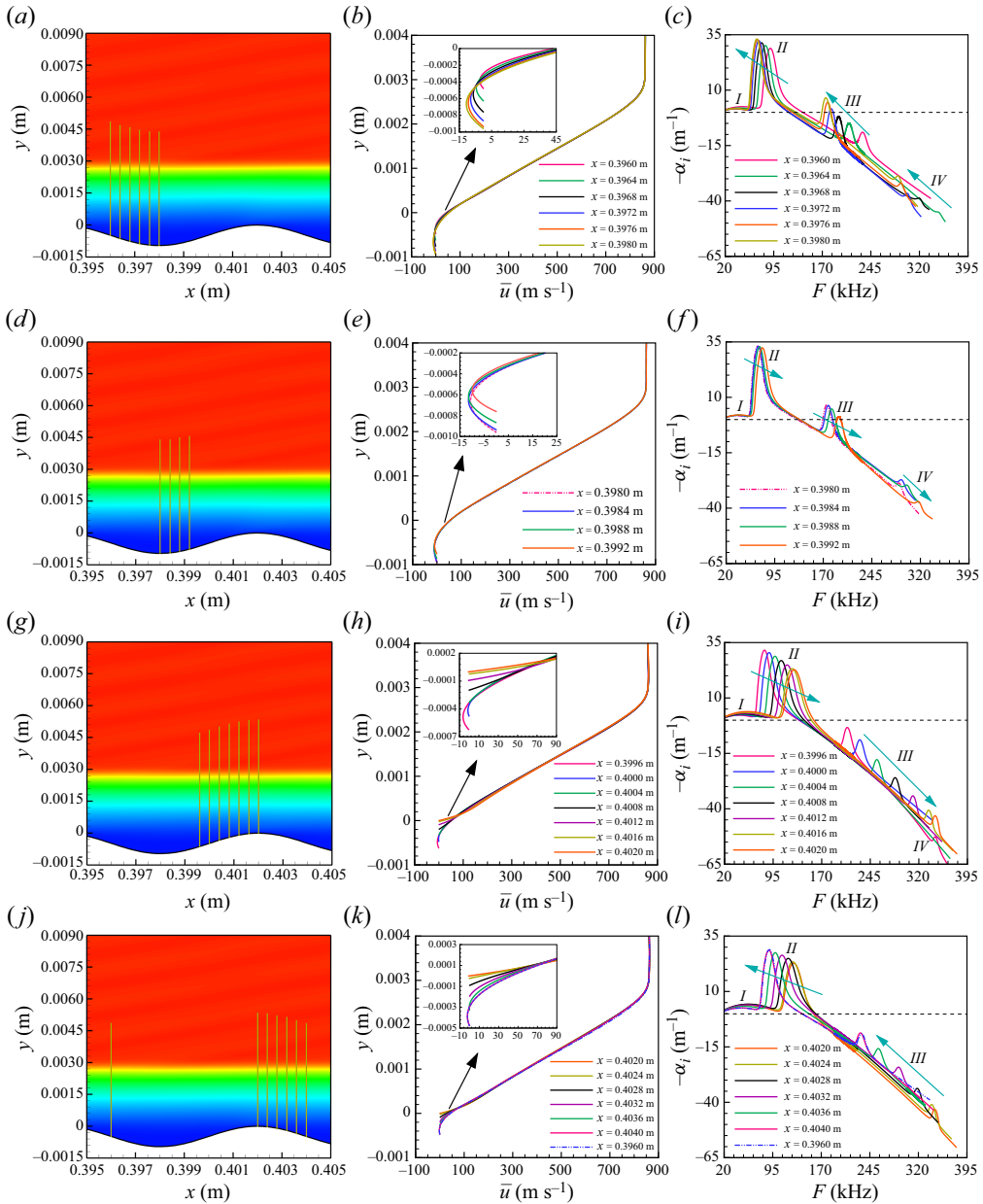
Figure 9. (*b,e,h,k*) Variation of streamwise velocity along the wall-normal direction at various locations across the roughness element centred at $x = 0.4$ m. (*a,d,g,j*) The roughness element for this case W2A2 with the background contours of the Mach number. (*c,f,i,l*) Amplification rates plotted as a function of disturbance frequency.

The six remaining locations, beginning at the crest of the roughness element, are shown in figure 9(*j*). The velocity profiles presented in figure 9(*k*) demonstrate that, as the height of the roughness increases, there is a corresponding rise in both the degree of flow separation and the effective boundary-layer height. This trend is consistent with observations from the locations depicted in figure 9(*a*). Furthermore, the growth rates of the second and third instability peaks show an increase as we progress downstream,

1008 A52-15

resulting in a shift of the unstable region towards lower-frequency ranges. In contrast, the amplification rate of peak I initially rises until reaching $x = 0.4028$ m, after which it declines to align with the growth rate variation observed at the starting position of the roughness element ($x = 0.3960$ m), as indicated by the blue dashed-dotted line in figure 9(l).

4.3.2. *Effect of pressure gradient and boundary-layer height*

Figure 10(a,c,e) plots the variation of the maximum growth rate of the instability peaks I, II and III along with the corresponding frequency for the roughness element shown in figure 9. Both growth rate and frequency show a similar variation for the case of instability peak I, whereas II and III show an inverse relationship between the two quantities. The maximum growth rate of peaks II and III scales with the effective boundary-layer height (see figure 10d,f). The effect of streamwise pressure gradient on the peak amplification rate of the instability peak I is shown in figure 10(b). Initially ($< 20\,\%\lambda$), we notice a reduction in the amplification rate due to a reduction in the pressure gradient; however, as the pressure increases along the roughness wavelength, the growth rate shows a sharp increase. Beyond $80\,\%\lambda$, the pressure gradient slowly reduces again, causing a reduction in the peak growth rate of instability peak I.

4.3.3. *Identification of dominant instability modes*

It can be observed from figure 9(c) that the maximum growth rates of instability peaks I, II and III at $x = 0.3980$ m occur at 35, 68 and 175 kHz, respectively. To identify the instability modes associated with these frequencies, we computed the eigenspectrum and plotted the real and imaginary part of the phase speed in figure 11. As illustrated in figure 11(a), the slow mode S emerges as the dominant instability mode at a frequency of 35 kHz, which corresponds to Mack's first mode. The terminology utilised for the discrete modes follows the framework established by Fedorov & Tumin (2011). The pressure eigenfunction is plotted over a disturbance wavelength corresponding to mode S in figure 11(b). The vertical coordinate η is computed using the Blasius viscous length scale at $x = 0.3980$ m. The amplitudes of pressure and temperature eigenfunction normalised by their maximum values are shown in figure 11(c) for the first mode. The peak value of the temperature eigenfunction appears closer to the critical layer ($M_r = (\bar{u} - c_r)/\sqrt{\gamma R \bar{T}} = 0$), indicated by the black dashed-dotted line.

As the frequency increases to 68 kHz, the fast mode F_1^- crosses the vorticity branch with phase speed $c_r = 1$ and synchronises with Mack's first mode S (see figure 12a). This leads to a significant increase in the growth rate of mode S, as can be observed from figure 12(b), which becomes Mack's second mode after the synchronisation. Therefore, the instability peak II that appeared in figure 9 at 68 kHz can be attributed to Mack's second mode and the corresponding eigenspectrum is presented in figure 11(d) at $x = 0.3980$ m.

The contours of disturbance pressure in figure 11(e) depict that acoustic waves become trapped between the wall and the relative sonic line ($M_r = -1$), as indicated by the black dashed line. Notably, the real component of the pressure eigenfunction changes sign only once within the boundary layer, thereby confirming its classification as the second mode. In contrast, the temperature eigenfunction peaks at the critical layer (cf. Figure 11f), while the pressure eigenfunction reaches its maximum at the wall.

Since the frequency ($F \approx \bar{u}_e / 2\delta_{0.99}$, where $\bar{u}_e$ represents the edge velocity) of the second mode is a function of the boundary-layer thickness $\delta_{0.99}$, we observed a shift in the instability peak II to lower or higher frequencies in figure 10(c) depending on whether the
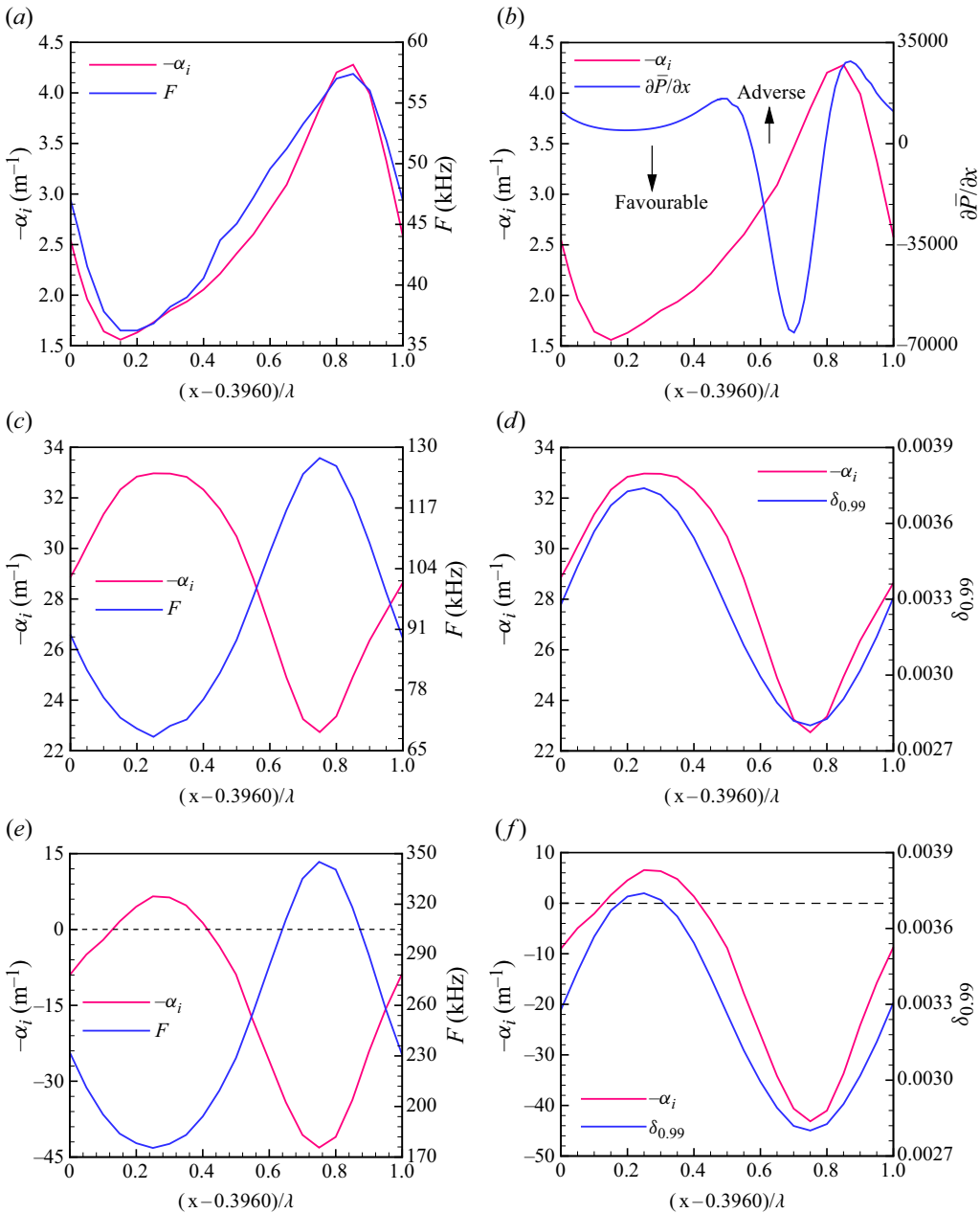
Figure 10. Variation of peak growth rate and frequency for the instability peaks (*a*) I, (*c*) II and (*e*) III as a function of the roughness wavelength centred at $x = 0.4$ m. (*b*) The streamwise pressure gradient over the roughness element and the peak growth rate for the instability peak I are shown. The variation of the maximum growth rate of (*d*) II and (*f*) III, along with the boundary-layer thickness.

effective boundary-layer height was increased or decreased, respectively (see figure 10*d*) while moving along the roughness element in figure 9.

As the frequency is increased further, the growth rate of the second mode decreases gradually and at $F = 175$ kHz, it synchronises with the fast mode F_2^+ (see figure 12*a*), which generates Mack's third mode (see figure 11*g*). Therefore, the third mode is
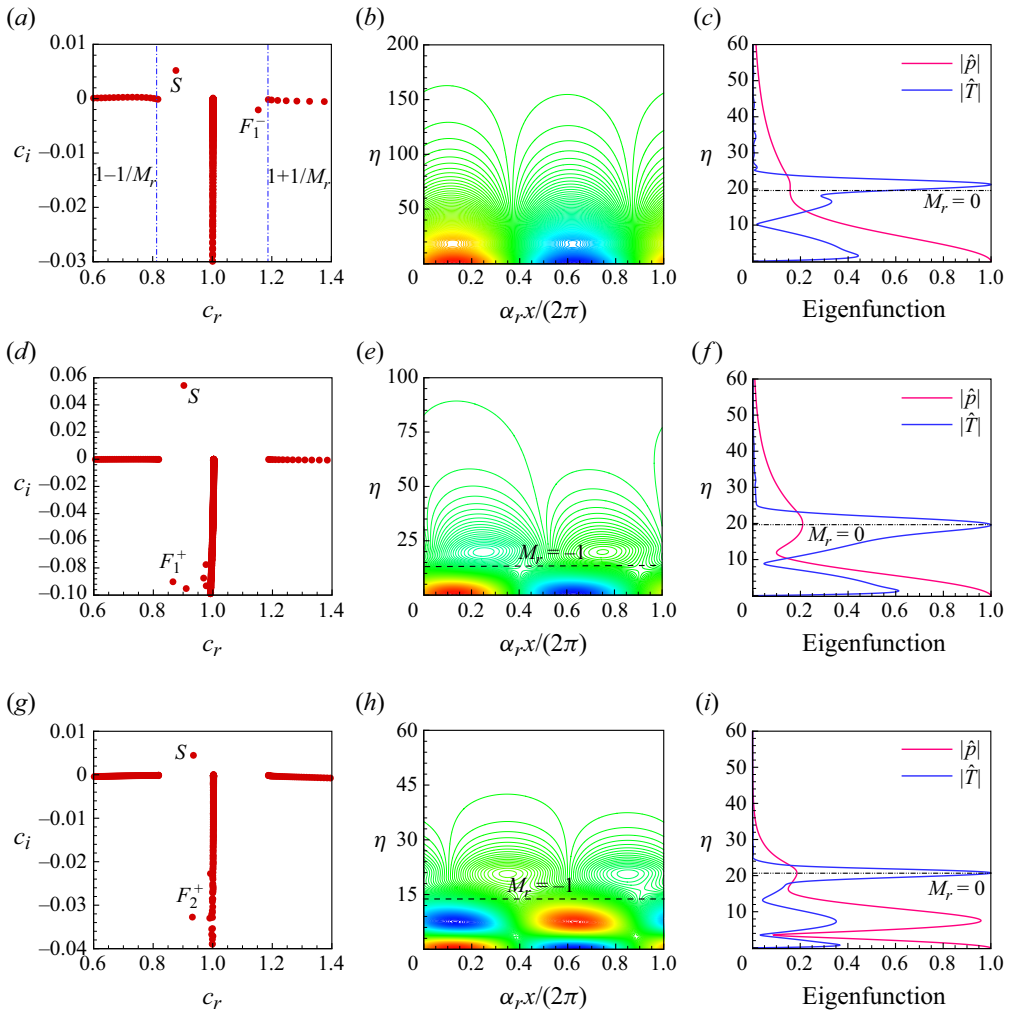
Figure 11. Eigenvalues are plotted in the complex phase-speed plane for the rough-wall case W2A2 corresponding to frequencies (*a*) 35 kHz, (*d*) 68 kHz and (*g*) 175 kHz at $x = 0.3980$ m. (*b,e,h*) Contours of disturbance pressure plotted over a wavelength of mode *S*. (*c,f,i*) Amplitudes of temperature and pressure eigenfunctions for mode *S* are shown at each frequency after normalising by the maximum value.

responsible for the instability peak III in figure 9. It can be noted that throughout the frequency range considered, the instability is caused by the slow mode *S*, whereas the fast modes remain stable. Like the second mode, the third mode is also trapped between the sonic line $M_r = -1$ and the wall, as seen from figure 11(*h*). The pressure eigenfunction changes sign twice, confirming it to be Mack's third mode. In addition to the largest peak at the critical layer, the temperature eigenfunction shows two more peaks close to the wall as opposed to one in the case of the second mode (see figure 11*i*). The frequency corresponding to the third mode is also a function of the boundary-layer thickness similar to the second mode, as shown in figure 10(*e,f*).

4.3.4. *Comparison with the smooth flat plate*

To investigate the impact of distributed roughness on growth rate variation with frequency, we conducted a comparative analysis of amplification rates at two specific locations along
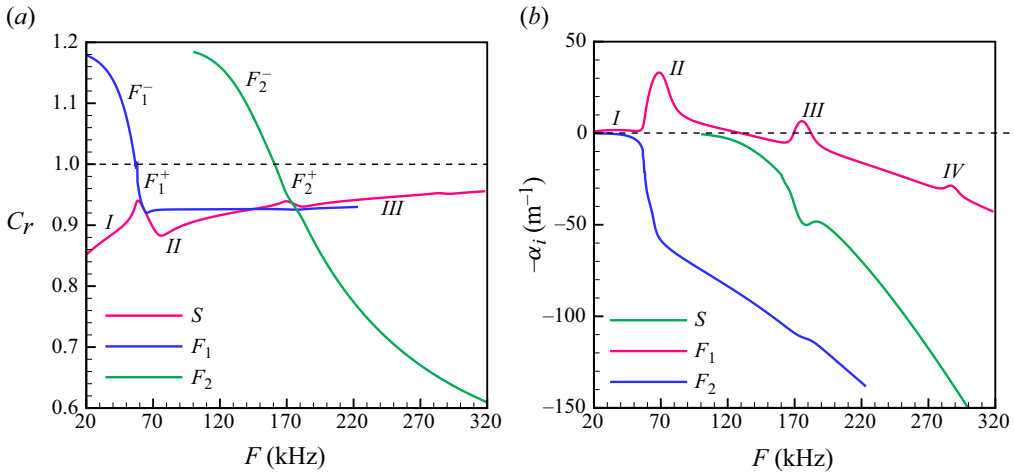
Figure 12. Variation of (*a*) phase speed and (*b*) growth rate for the slow and fast modes plotted as a function of frequency for the rough-wall case W2A2 at $x = 0.3980$ m.
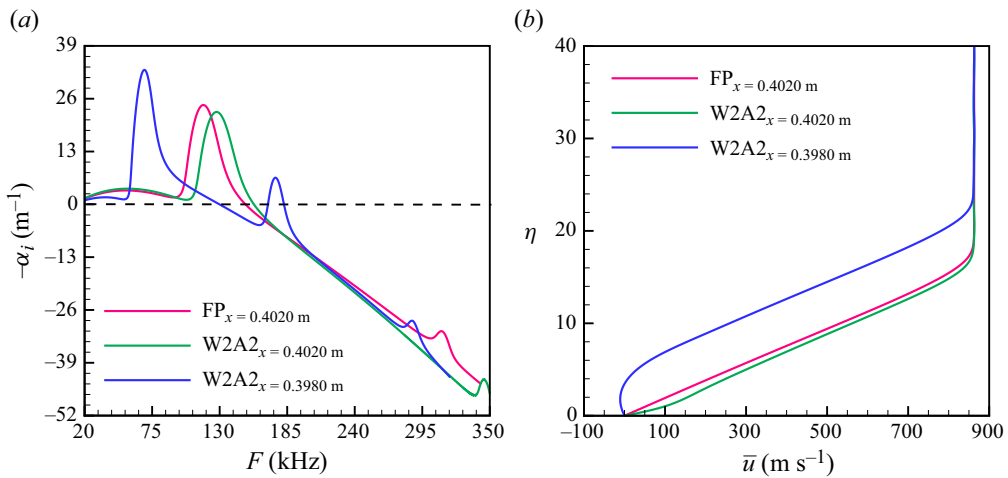

Figure 13. (*a*) Comparison of spatial growth rate computed at two streamwise locations for the rough-wall case W2A2 with the smooth-wall data at $x = 0.4020$ m. (*b*) The corresponding mean-flow streamwise velocity profiles.

the roughness wavelength corresponding to the rough-wall case W2A2, contrasting these findings with the data obtained under smooth-wall conditions, as illustrated in figure 13(*a*). The initial comparison location is $x = 0.4020$ m, positioned at the crest of the roughness element (see figure 9*j*). The variation of mean-flow profiles at this location is very similar to the smooth-wall case, albeit with a slightly lower boundary-layer thickness (see figure 13*b*).

The region of relative supersonic flow exhibits a slightly greater extent in the case of the smooth flat plate, as indicated by the movement of the sonic line $M_r = -1$ from $\delta_{sl} = 7.94$ in the rough-wall configuration to $\delta_{sl} = 8.49$ for the smooth-wall case (details not shown in the figure). Consequently, while the variation in the amplification rate remains consistent regarding the presence of Mack modes, the frequencies associated with the second and third instability peaks shift to a slightly lower range for the smooth flat plate.

It is important to note that, contrasting with the influence of wall cooling – where the boundary layer thickens as a result of increased mean-flow density within the boundary layer, resulting in a shift of the second mode to a higher-frequency range with an enhanced peak growth rate – this scenario presents a reduction in the growth rate when the boundary-layer thickness is decreased (refer to figure 10*d*). Nonetheless, the shift of the growth rate peak to higher frequencies with a reduction in boundary-layer height (as illustrated in figure 10*c*) behaves similarly to the effects observed with wall cooling. The influence of distributed roughness on the growth rate of the higher Mack modes is analogous to the effects observed with wall blowing. In both scenarios, an increase in boundary-layer thickness results in a higher amplification rate (Saikia & Brehm 2024).

The subsequent location selected for analysis is $x = 0.3980$ m, situated at the trough of the roughness element (refer to figure 9*a*). In the case of a smooth wall, the mean-flow profiles exhibit minimal variation between $x = 0.3980$ and 0.4020 m, which results in a comparable growth rate at both locations. However, as demonstrated in figure 13(*b*), the effective boundary-layer thickness at $x = 0.3980$ m is considerably greater for the rough-wall scenario when contrasted with the smooth flat plate. This increase leads to a larger relative supersonic region ($M_r \leqslant -1$) for the W2A2 case. As a result, the frequencies of the acoustic waves confined within the supersonic region decrease substantially, which subsequently causes the instability peaks related to the second and third modes to shift towards a notably lower-frequency range (see figure 13*a*). Moreover, Mack's fourth mode emerges at higher frequencies (≈ 286 kHz) for the rough-wall case, appearing at a slightly lower frequency than the third mode observed for the smooth-wall case.

4.3.5. *Scaling of the instability peaks*

As the variation of growth rate changes, while traversing a roughness element, we aimed to identify a parameter that effectively scales the disturbance frequency, allowing the instability peaks at each location to converge on a single non-dimensional frequency. To exemplify this concept, we selected three x locations along the roughness element centred at $x = 0.4$, corresponding to the rough-wall case W2A3. The growth rate variations at these locations are presented in figure 14(*a*).

Given that the frequency of the second mode scales inversely with boundary-layer thickness, we computed the boundary-layer thickness using velocity profiles illustrated in figure 14(*b*). We observed a reduction in the boundary-layer height, decreasing from 4.23 to 2.78 mm as we moved from $x = 0.3980$ to 0.4016 m. By applying the boundary-layer thickness $\delta_{0.99}$ and the edge velocity $\bar{u}_e$, we determined the non-dimensional frequency $F_{\delta_{0.99}}$ at each location, calculated as $F_{\delta_{0.99}} = F/(\bar{u}_e/\delta_{0.99})$. Figure 14(*e*) displays the variation of growth rate as a function of the non-dimensional frequency $F_{\delta_{0.99}}$. Although the instability peaks associated with the second and third modes demonstrate a closer alignment when utilising the non-dimensional frequency, as depicted in figure 14(*a*), they do not converge to a singular frequency. Moreover, the application of the thermal boundary-layer height, in lieu of the velocity boundary-layer thickness, similarly does not result in the collapse of the instability peaks into a single non-dimensional frequency (not shown here).

The presence of a relative supersonic region is critical for the manifestation of Mack modes, as outlined in previous studies (Mack 1975, 1984, 1987). Consequently, the distance from the wall to the sonic line, denoted by $M_r = -1$, can serve as an effective parameter for non-dimensionalising disturbance frequency. The variation of the relative Mach number across the boundary layer is presented in figure 14(*c*). The intersection of the black dashed-dotted line with the M_r profile signifies the wall-normal position of the sonic

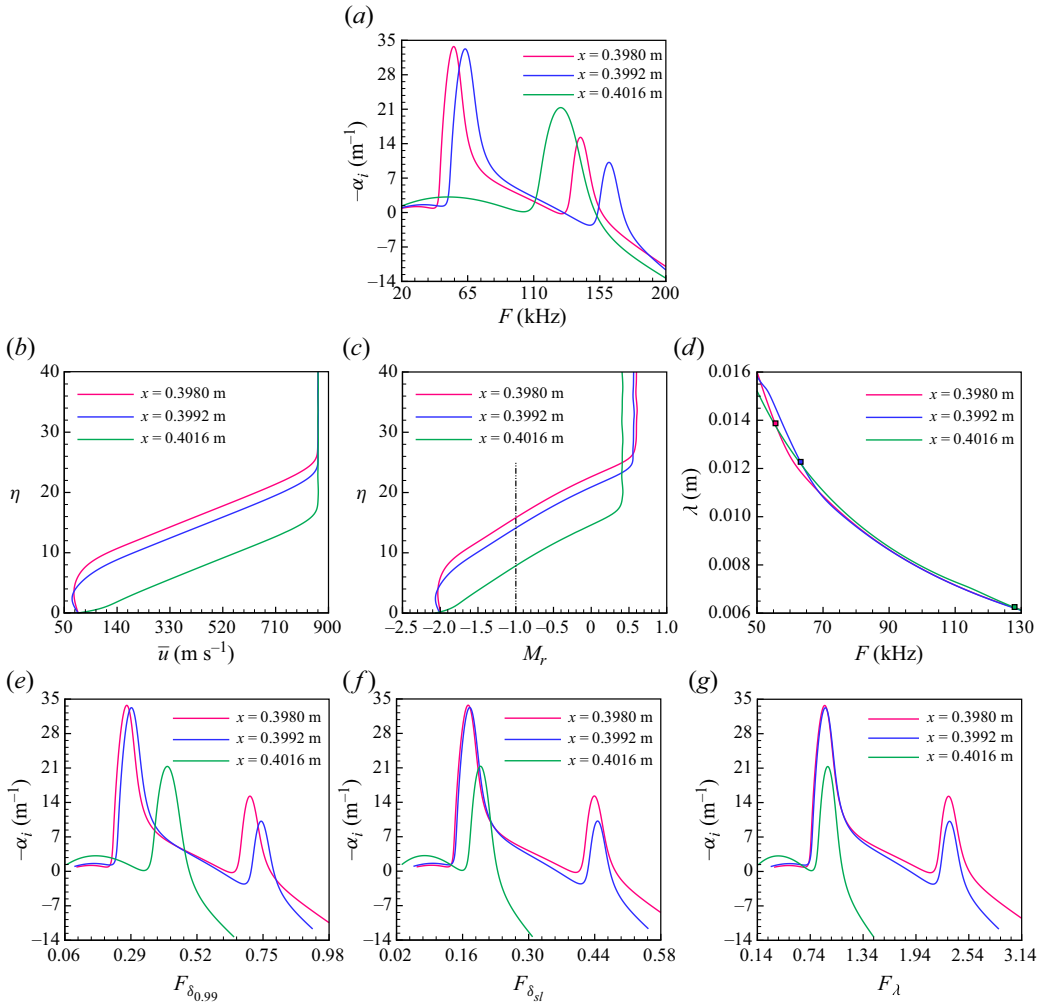Figure 14. (*a*) Amplification rate and (*d*) second-mode wavelength are plotted as a function of frequency at three *x* locations along the roughness element centred at $x = 0.4$ m for the W2A3 case. The (*b*) streamwise velocity and (*c*) relative Mach number are plotted along the wall-normal direction. Growth rates as a function of the non-dimensional frequency obtained after normalising by (*e*) the boundary-layer thickness, (*f*) sonic line height and (*g*) second-mode wavelength.

line. Consistent with the behaviour of the velocity boundary-layer height, the distance to the sonic line diminishes from $x = 0.3980$ to $x = 0.4016$ m, indicating a reduced relative supersonic region at the later streamwise location.

Utilising the height of the sonic line, δ_{sl}, the non-dimensional frequency for each case is calculated as $F_{\delta_{sl}} = F/(\bar{u}_e/\delta_{sl})$. The resulting variation of amplification rates at each location in relation to the non-dimensional frequency $F_{\delta_{sl}}$ is depicted in figure 14(*f*). The distance from the sonic line to the wall appears to serve as a more effective parameter for frequency normalisation compared with $\delta_{0.99}$, as evidenced by the nearly perfect alignment of peaks corresponding to the second mode at the first two locations. Furthermore, a significant shift in the second instability peak at $x = 0.4016$ m has been observed, bringing it closer to the other two locations along the x axis. Nonetheless, both δ_{sl} and the critical

layer height (not included in this discussion) have yet to yield a collapse of the growth rate variation against the non-dimensional frequency.

The inability to achieve a collapse of the second-mode growth rate suggests that the frequency does not scale effectively with the thermal and velocity boundary-layer thickness nor with the relative height of the sonic line or critical layer. To investigate this phenomenon further, we calculated the second-mode wavelength corresponding to frequencies that yield the maximum amplification of this mode at three designated x locations. The resulting variation in disturbance wavelength, derived from the phase-speed equation ($\lambda = c_r/F$), is illustrated as a function of frequency in figure 14(d). The square markers indicate the second-mode wavelength associated with the frequency that produces the highest amplification at each location. The figure demonstrates a significant reduction in the second-mode wavelength, decreasing from $\lambda = 0.0139$ m at the first location to 0.0062 m at the third location. Consistent with the previous cases, the non-dimensional frequency was calculated using this second-mode wavelength and is defined as $F_\lambda = F/(\bar{u}_e/\lambda)$. Figure 14($g$) illustrates that the parameter F_λ facilitates a notably improved collapse of the second mode across all three x locations. Additionally, this parameter effectively collapses the peak for the third mode at the first two locations.

4.3.6. *A comparison between LST and LDS data*

To evaluate the efficacy of LST in characterising the stability properties of boundary-layer flow in the presence of distributed roughness, we conducted an analysis of the amplification rates at various locations along the roughness element centred at $x = 0.4$ m. This analysis was performed for all amplitude-varying cases similar to the W2A2 case described in § 4.3.1. In figure 15(a,c,e,g), the blue and black lines represent the growth rates measured at the initial location ($x = 0.3960$ m) and the final location ($x = 0.4036$ m) along the roughness element, respectively.

Our findings indicate significant variability in the growth rates along the roughness element for each amplitude-varying case, attributable to considerable changes in the mean flow between different streamwise locations. For the smallest roughness case, W2A1, illustrated in figure 15(a), the second-mode instability region is observed to span frequencies from 75 to 160 kHz, with an increase in roughness height correlating to an expansion of this instability region. In contrast, for the largest-roughness case, W2A4, presented in figure 15(g), the unstable region associated with the second mode initiates at a significantly lower frequency ($= 35$ kHz) and extends to 167 kHz. Notably, in the smallest-roughness case, only the first and second modes are detected within the selected frequency range, while the larger-amplitude cases additionally reveal the presence of Mack's third mode (see figure 15c,e,g).

The magenta line depicts the averaged growth rate calculated across the roughness wavelength based on the LST data. Figure 15(b,d,f,h) compares this averaged growth rate variation across each amplitude-varying case with the roughness-wavelength-averaged LDS data. For the smallest-roughness case shown in figure 15(b), the unstable region predicted by LST slightly exceeds the numerical data, with the second-mode instability extending to a marginally higher frequency in this scenario.

It is important to highlight that the LDS data undergo an initial adjustment due to the presence of multiple modes, which are characterised by oscillations in the lower-frequency range. As a result, discerning the growth rate in the region dominated by the first mode from the LDS data proves to be challenging, as these oscillations impact the growth rate

plot. Furthermore, as illustrated in figure 15(*b*), there exists a discrepancy in the peak growth rate of the second mode between LST and LDS data. This discrepancy can be attributed to the limitations of the LST method in capturing non-parallel effects.

As illustrated in figure 15(*d*), increasing the roughness height to 20.9 % of the boundary-layer thickness results in the averaged growth rate from LST exhibiting an additional peak at 114 kHz, alongside the existing second-mode peak at 74 kHz. It should be noted that this peak does not correspond to Mack's third mode, but it is still the second mode. It appears due to a shift in the second-mode instability peak to higher frequencies at certain *x* locations as shown in figure 15(*c*).

While the third mode for the W2A2 case appears at a significantly higher frequency (= 176 kHz), it does not contribute to amplification on average. Additionally, the variation in the averaged growth rate within the second-mode-dominated region includes some contributions from the first mode, which is detectable up to a frequency of 104 kHz. In contrast to the smallest-roughness case, LDS data indicate a slightly broader second-mode instability region compared with the LST results (see figure 15*d*). Furthermore, a notable decrease in the amplification of the second mode is observed when comparing the averaged LST growth rate with the LDS results. The third instability peak identified in the numerical simulation occurs at a significantly higher frequency (= 152 kHz) than that predicted by LST.

As the roughness height is increased further, the averaged growth rate at the peaks predicted by LDS reduces, and they follow more closely the growth rate variation obtained from LST over the considered frequency range (see figure 15*f*,*h*). Similar to the W2A2 case, the second-mode growth rate peak which is observed around 60 and 51 kHz for the larger-roughness cases W2A3 and W2A4, respectively, is a result of both the first- and the second-mode growth (see figure 15*e*,*g*). The unstable regions which occur above 130 and 109 kHz for the rough-wall cases W2A3 and W2A4, respectively, are due to both second- and third-Mack-mode growth, with the major contribution coming from the second mode. Two instability peaks are also observed in the LDS data in a similar frequency range to that predicted by LST in figure 15(*h*), indicating the presence of the Mack modes. Therefore, the unstable region observed for all the amplitude-varying cases in figure 6 is mainly due to the amplification of the second mode. The branching observed at higher frequencies in figure 6(*d*,*e*) is simply the consequence of the appearance of Mack's third mode on top of the second-mode-dominated region.

Finally, a comparison of the averaged amplification rates for the amplitude-varying cases obtained from LST is shown in figure 16(*a*), and the corresponding growth rates computed from Fourier-transformed wall-pressure data from LDS are presented in figure 16(*c*). Although there is a difference in the amplification rates, a similar shift in the second-mode peak to a lower-frequency range with increasing roughness height is evident in both data sets. The growth rates are also depicted as a function of disturbance frequency, normalised by the second-mode wavelength corresponding to its maximum amplification. Similar to the W2A3 case outlined in figure 14(*g*), where growth rates converge to a single non-dimensional frequency across three streamwise locations above a roughness element, figure 16(*b*,*d*) further demonstrates that the peaks of second-mode instability, associated with all amplitude-varying cases, can be effectively collapsed into a single non-dimensional frequency for both LST and LDS data.

5. Effect of roughness wavelength

The wavy-wall stabilisation concept proposes the substitution of long separation bubbles with a series of smaller ones to mitigate any adverse acoustic resonances within these
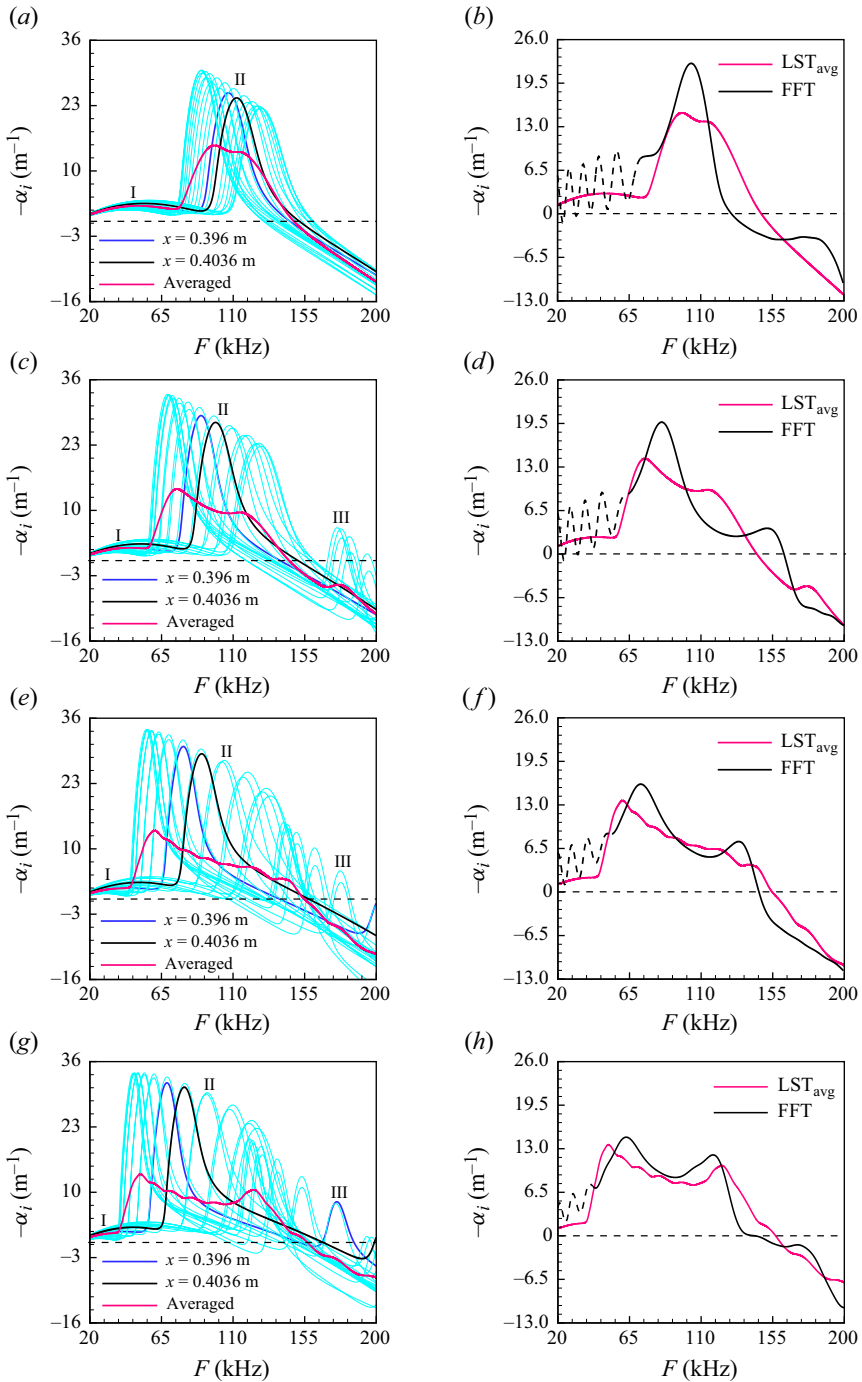
Figure 15. The variation of the LST growth rate with frequency plotted across a roughness wavelength centred at $x = 0.4$ m, with the blue and the black lines denoting the amplification rates corresponding to the first and the last location of the roughness element, respectively, for cases (*a*) W2A1, (*c*) W2A2, (*e*) W2A3 and (*g*) W2A4. The magenta line corresponds to the averaged growth rate computed over the roughness wavelength using the LST solver, and (*b*,*d*,*f*,*h*) it is compared with the averaged LDS growth rate for each amplitude-varying case shown in the left-hand column.
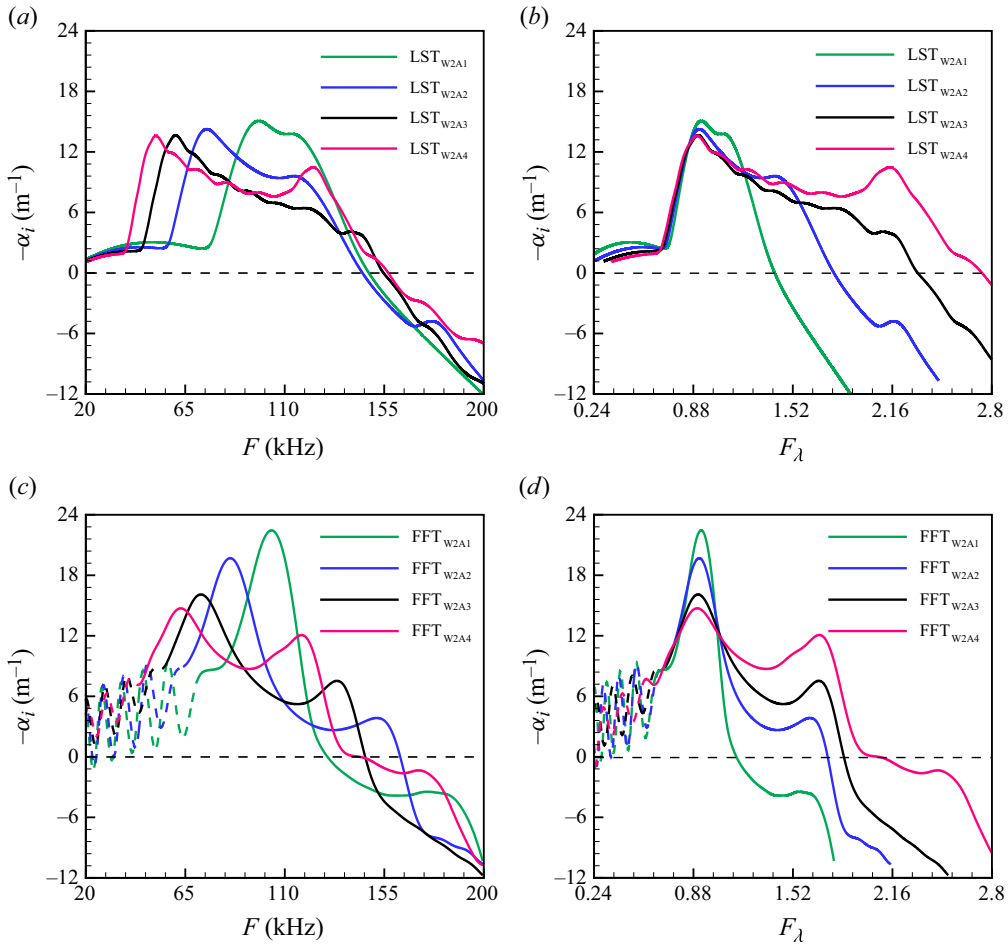
Figure 16. Effect of increasing the roughness height on the averaged spatial growth rate over a roughness element centred at $x = 0.4$ m plotted as a function of the disturbance frequency computed using (*a*) LST and (*c*) LDS. (*b,d*) The same growth rate plotted after normalising the frequency by the disturbance wavelength corresponding to the peak second-mode growth.

bubbles. Research indicates that the second mode is effectively damped by the stabilising influence of a relatively long free shear layer that develops atop a streamlined surface, as established by Bountin *et al.* (2013). A numerical investigation conducted by Zhou *et al.* (2017) corroborated this concept, revealing that a rough wall featuring multiple wavenumbers can substantially suppress the growth of the second mode compared with a rough wall with a single wavenumber. In this section, we review the rough-wall stabilisation concept utilising sinusoidal roughness elements with wavelengths ranging from shorter ($0.87\delta_{0.99}$ at $x = 1$ m corresponding to the smooth flat plate) to longer ($6.96\delta_{0.99}$), corresponding to the test cases outlined in table 2.

5.1. *Mean flow field*

The steady mean flow fields corresponding to the wavelength-varying cases are shown in figure 17 in terms of pressure contours. The streamwise domain depicted in the figure encompasses the first six roughness wavelengths for each case. Consistent with the amplitude-varying cases discussed in the previous section, the roughness elements
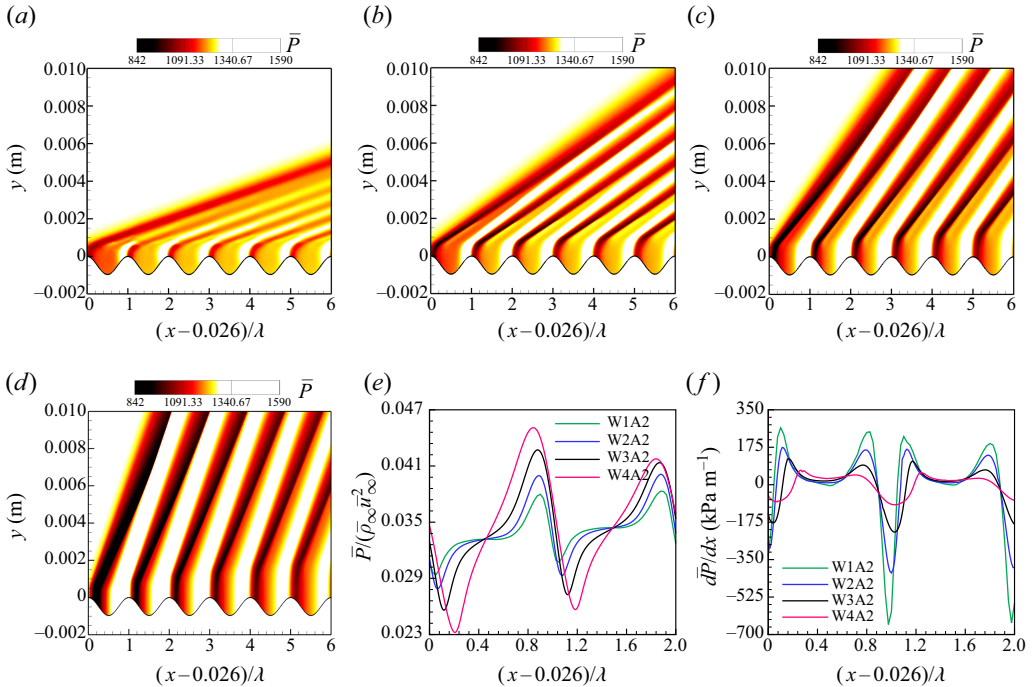
Figure 17. Contours of pressure showing the mean flow field above the first six roughness elements corresponding to (*a*) W1A2, (*b*) W2A2, (*c*) W3A2 and (*d*) W4A2. Variation of (*e*) non-dimensional mean-flow pressure and (*f*) streamwise pressure gradient along the first two roughness elements extracted at $y = 0$ for the wavelength-varying cases.

commence at $x = 0.026$ m, where the first expansion fan is observed, as indicated by the dark black contours. The flow fields demonstrate similarities to those presented in figure 2 regarding the expansion and compression waves generated at the surface. Notably, the primary effect of increasing the roughness wavelength is the enhancement of the strength of the expansion and compression waves generated by the roughness elements.

A comparison of the normalised mean-flow pressure measured at $y = 0$ above the first two roughness elements across all four rough-wall cases is presented in figure 17(*e*). The findings reveal substantial variations in the mean-flow characteristics for all cases with differing wavelengths, with increases in peak pressure values corresponding to longer roughness wavelengths. This observation is further supported by the streamwise pressure gradient variations illustrated in figure 17(*f*), which show that the case with the smallest wavelength yields the most favourable pressure gradients.

The d-type roughness behaviour is evident across all cases in figure 18, with the exception of the largest-wavelength case, which exhibits k-type separation (as illustrated in figure 18*d*). An increase in roughness wavelength results in a more gradual transition of the pressure gradient, with a reduced magnitude, as demonstrated by the largest-wavelength case in figure 17(*f*). This leads to a smaller separation bubble in relation to the height of the roughness. Furthermore, this alteration causes the shear layer to bend inward, approaching the wall, in contrast to the nearly parallel shear layer that characterises the smaller-wavelength cases, where the shear layer connects smoothly across the crests of the neighbouring roughness elements.

The variation of normalised streamwise velocity and temperature is plotted along the boundary layer in figures 19(*a*) and 19(*b*), respectively, after averaging over a roughness
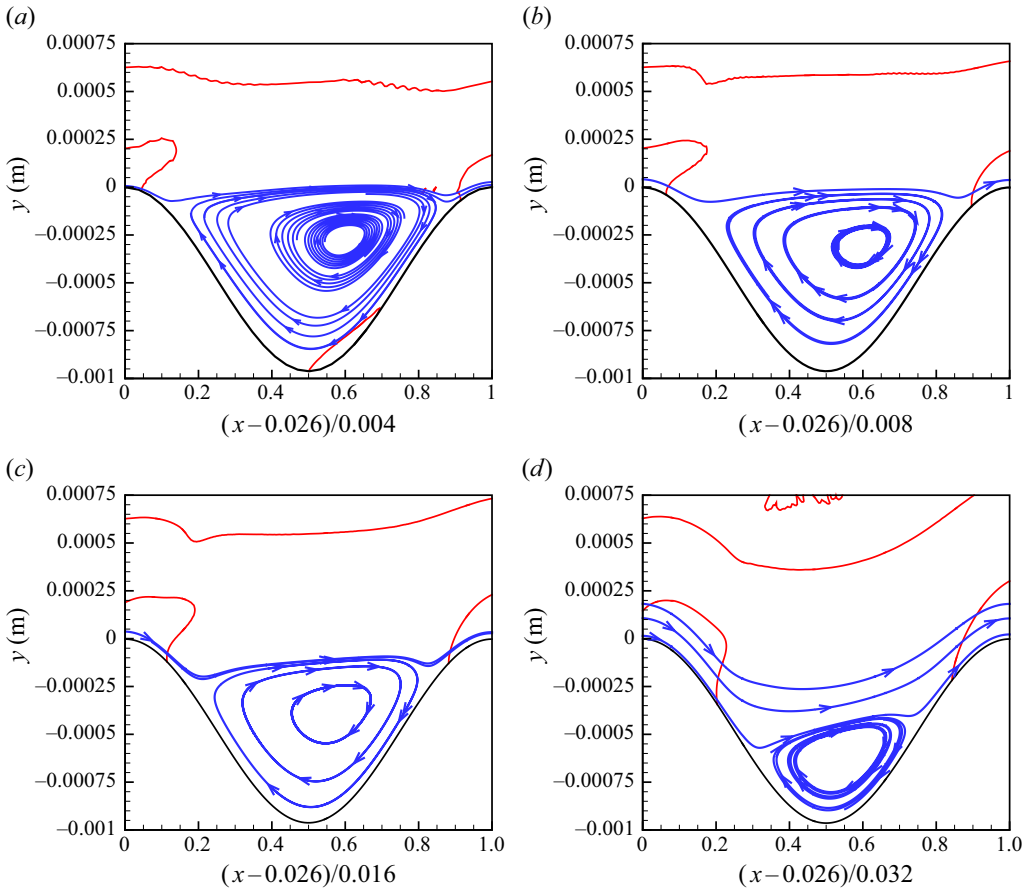
Figure 18. Streamlines showing the flow separation region along the first roughness wavelength corresponding to (*a*–*d*) the four wavelength-varying cases from table 2. The background red lines denote the zero contours of inflectional profile $\partial/\partial y(\bar{\rho}(\partial \bar{u}/\partial y))$.
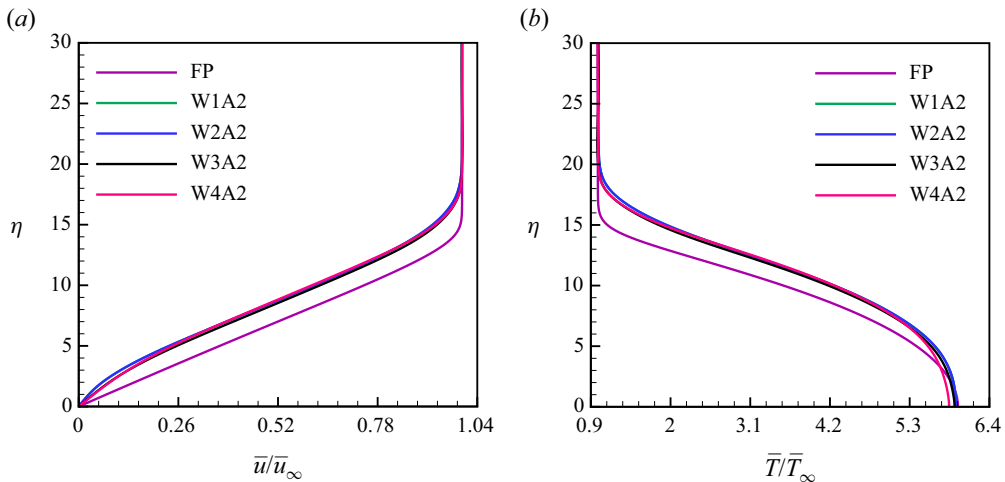

Figure 19. Comparison of normalised (*a*) velocity and (*b*) temperature profiles averaged over a roughness wavelength for the four wavelength-varying cases compared with the smooth-wall data extracted at $x = 0.4$ m.
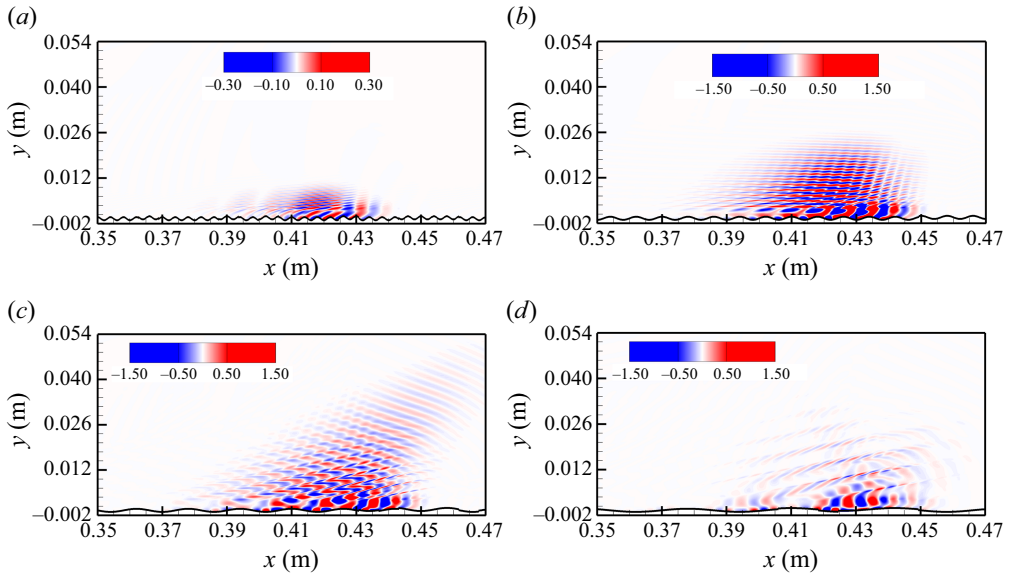
Figure 20. Effect of variation of roughness wavelength on the disturbance pressure flow field for the four rough-wall cases (*a*) W1A2, (*b*) W2A2, (*c*) W3A2 and (*d*) W4A2.

wavelength centred at $x = 0.4$ m for the rough-wall cases. Compared with the smooth-wall data, all the wavelength-varying cases show an increase in the momentum and the thermal boundary-layer thickness. Since all the rough-wall cases have the same roughness height, they all lead to a similar boundary-layer thickness.

5.2. *Disturbance flow field*

Utilising the steady base flows outlined in the previous subsection, we computed the disturbance flow fields for the wavelength-varying cases by introducing a 100 kHz pulse, as detailed in § 3. The disturbance flow field is represented through pressure contours in figure 20. Given that the contour legend is anchored around the same minimum and maximum values as in the smooth-wall case presented in figure 1(*b*), it is observed that the rough-wall case W1A2, with a roughness wavelength of $0.87\delta_{0.99}$, results in a slight reduction in pressure values (see figure 20*a*). The interaction of disturbances near the wall with Mach waves generates streaky structures on top of the wave packet.

As the roughness wavelength approaches the second-mode wavelength, a pronounced amplification of disturbance pressure is evident in figure 20(*b*), corresponding to the W2A2 case. It is plausible that a resonance mechanism is activated when both wavelengths are of comparable length, leading to an increased amplification of the disturbances, with the streaky structures over the roughness elements becoming more pronounced.

When the roughness wavelength is increased to approximately twice that of the second mode wavelength in the W3A2 case, a slight decline in pressure values is noted compared with the preceding case. Nevertheless, the interaction between the near-wall disturbances and the Mach waves extends significantly farther from the wall (see figure 20*c*). A further increase in the roughness wavelength results in a marked reduction in both the streaky structures and the disturbance pressure values, as illustrated in figure 20(*d*). As the roughness wavelength continues to increase, the stability characteristics may begin to resemble those of a smooth-wall flat plate.
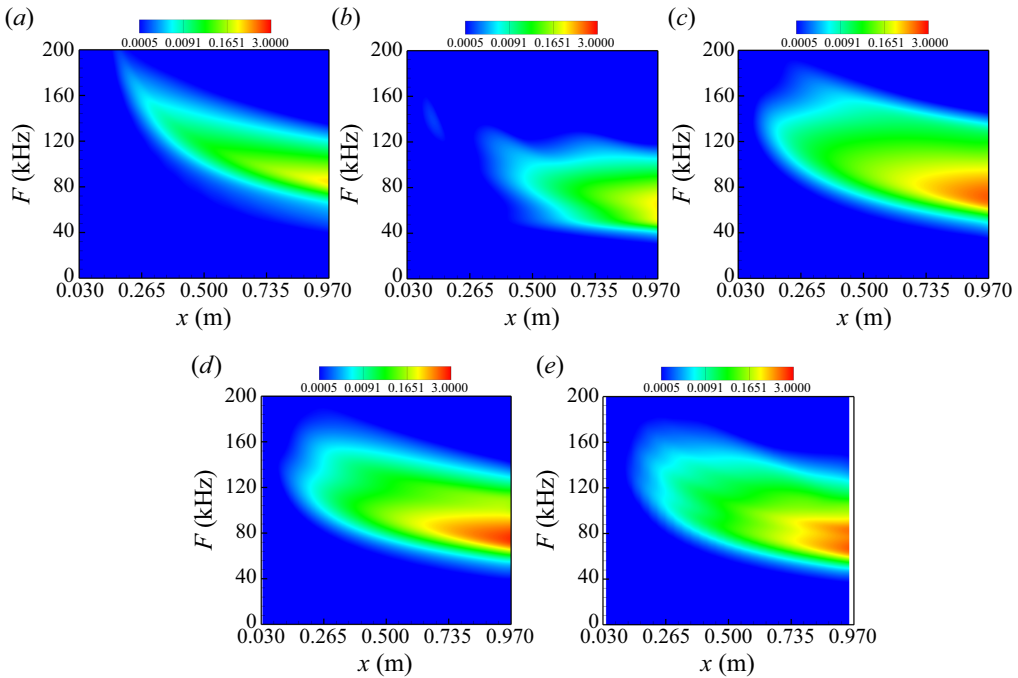
Figure 21. Fourier-transformed disturbance wall-pressure amplitude for (*a*) the smooth-wall case compared with the different roughness wavelength cases (*b*) W1A2, (*c*) W2A2, (*d*) W3A2 and (*e*) W4A2.

A FFT of the wall-pressure data in the time domain is performed to determine the range of frequencies leading to the maximum growth of near-wall disturbances for the wavelength-varying cases. The logarithmic representation of the pressure amplitude data corresponding to the largest-wavelength case W4A2 is shown in Appendix A. Since both amplitude and growth rate show large variations due to the presence of roughness elements (see figure 27*c*,*d*), they are averaged over each roughness wavelength. The averaged amplitudes for each wavelength-varying case are presented in figure 21 as a function of frequency and streamwise distance.

Compared with the smooth flat plate in figure 21(*a*), the lowest-wavelength case W1A2 shifts the pressure values to a much lower frequency range (see figure 21*b*). Disturbances start to amplify around 61 kHz for this rough-wall case, and the unstable region extends until a frequency of 118 kHz (see figure 22*a*). The amplitude loop shifts farther downstream along the plate compared with the smooth-wall case, leading to a significant reduction in the pressure values at $x = 0.4$ m (see figure 23*a*). The pressure amplitude demonstrates minimal values prior to this location for the case with the smallest wavelength; consequently, this location has been designated for comparison across all cases presented in figure 23(*a*). The instability region for the flat plate starts from 91 kHz at $x = 0.4$ m, and the flow becomes stable after 134 kHz. The amplitude data plotted close to the end of the domain in figure 23(*b*) show a large increase in the pressure amplitude compared with the previous location. A comparable peak amplitude is observed between the two cases at this location, although at a much lower frequency for the W1A2 case.

Increasing the roughness wavelength from 0.004 to 0.008 m enhances the pressure amplitudes significantly (see figure 21*c*). The rough-wall case W2A2 leads to the largest increase in the wall-pressure amplitude at $x = 0.4$ m (see figure 23*a*) There is also a significant increase in the growth rate compared with the lowest-wavelength case; however,
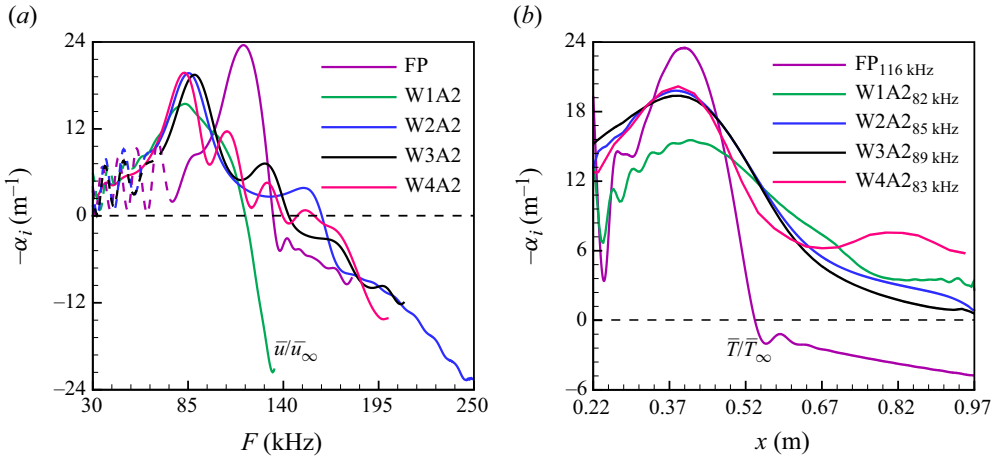
Figure 22. (*a*) Comparison of the averaged growth rate extracted at $x = 0.4$ m for the four wavelength-varying cases compared with the smooth-wall case as a function of the frequency. (*b*) Comparison of amplification rates along the wall corresponding to the frequencies leading to the maximum instability growth rate in (*a*).
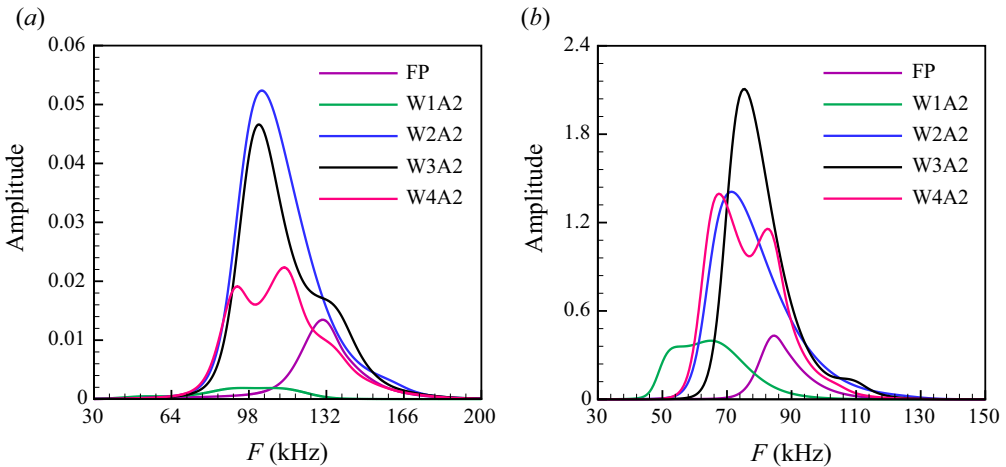

Figure 23. Comparison of the averaged pressure amplitude extracted at (*a*) $x = 0.4$ m and (*b*) $x = 0.97$ m plotted as a function of disturbance frequency.

it is much smaller than the smooth-wall data (see figure 22*a*). Starting from 61 kHz, the unstable region (above the dotted line in figure 22 with $-\alpha_i > 0$) extends to a much larger frequency due to the appearance of another instability peak at 150 kHz for W2A2.

Although the rough-wall case W3A2 with a roughness wavelength of $3.5\delta_{0.99}$ shows slightly lower pressure values at $x = 0.4$ m compared with the W2A2 case, it leads to the largest wall-pressure amplitude at the end of the domain (see figures 21*d* and 23*b*). There is an indication of another instability peak at 132 kHz in addition to the first peak, which is observed at 102 kHz for the W3A2 case in figure 23(*a*). This second peak can be easily identified in the growth rate plot in figure 22(*a*), where the appearance of this peak extends the unstable region. A shift in the second instability peak towards a lower-frequency range is observed with increasing roughness wavelength.

1008 A52-30

As the roughness wavelength is increased further, the second peak in pressure amplitude attains a slightly higher value as compared with the first peak for W4A2 at $x = 0.4$ m (see figure 23a). Although higher than for the smooth wall, both peaks still have a much smaller amplitude than the previous two rough-wall cases W2A2 and W3A2. These local peaks can be attributed to three almost merged pressure amplitude loops shown in figure 27(a) (see Appendix A) generated due to the modulation of mean flow due to surface roughness. At the end of the domain (see figure 23b), the largest-wavelength case shows a similar peak pressure value to that of the W2A2 case, with the first peak having a higher amplitude than the second one as opposed to the previous location. Although the first instability peak shows a similar amplification between both the cases, W4A2 displays two additional local peaks as can be observed from figure 22(a). The frequency corresponding to the second instability peak is shifted to a much lower value compared with W2A2 and W3A2 cases, albeit with a higher amplification. Similar to the effect of increasing the roughness height as shown in figure 7, multiple instability peaks are observed when the roughness wavelength is increased, and these peaks move to lower disturbance frequencies with larger roughness wavelengths.

To determine the extent of the unstable region for each case, the amplification rates are plotted in figure 22(b) after extracting them at frequencies corresponding to the largest growth rate at $x = 0.4$ m. Although the smooth-wall case is stable for $x > 0.53$ m, all the wavelength-varying cases are unstable throughout the entire computational domain. After attaining maximum amplification at $x = 0.4$ m, all the rough-wall cases except the largest-wavelength case show a gradual decrease in disturbance growth. Another local peak in growth rate is observed at $x = 0.8$ m for the rough-wall case W4A2.

Next, the wall-pressure amplitudes are converted to N-factors at multiple frequencies to determine how much amplification has occurred over the entire computational domain. The magenta line in figure 24(a–e) corresponds to the frequency leading to the maximum N-factor at the end of the domain. Compared with an N-factor of 9.34 for the smooth-wall case in figure 24(a), the lowest-wavelength case W1A2 leads to a lower N-factor of 8.54 (see figure 24b). The frequency corresponding to the maximum N-factor shifts from 84 kHz in the smooth-wall case to 66 kHz for the rough-wall case W1A2. An increase in the N-factor ($= 10.23$) is observed when the roughness wavelength approaches the second-mode wavelength. The frequency leading to the maximum N-factor also increases to 72 kHz in figure 24(c). Increasing the roughness wavelength further leads to a maximum N-factor of 11.12 corresponding to a disturbance frequency of 74 kHz for the W3A2 case in figure 24(d). The largest-wavelength case W4A2 shows the maximum N-factor ($= 10.3$) at a much lower frequency of 66 kHz. A comparison of the N-factor envelope for each wavelength-varying case is presented in figure 24(f) along with the smooth-wall data. The figure shows that the shortest distributed roughness can reduce the second-mode amplification compared with the smooth-wall case.

5.3. *Linear stability analysis for the wavelength-varying cases*

Since the dominant modes leading to the unstable regions in figure 21 have not been identified yet, we next computed the amplification rates using the spatial LST solver. For a roughness element centred at $x = 0.4$ m, these growth rates are plotted in figures 25(a)–25(c) corresponding to wavelength-varying cases W1A2, W3A2 and W4A2, respectively. Only the first and last locations represented by the blue and black lines are labelled, and other locations in between are shown in the same line colour. In the case of W1A2, the first-mode-dominated region is observed until a frequency of 76 kHz, which can be much shorter (<49 kHz) depending on the x location above the roughness element
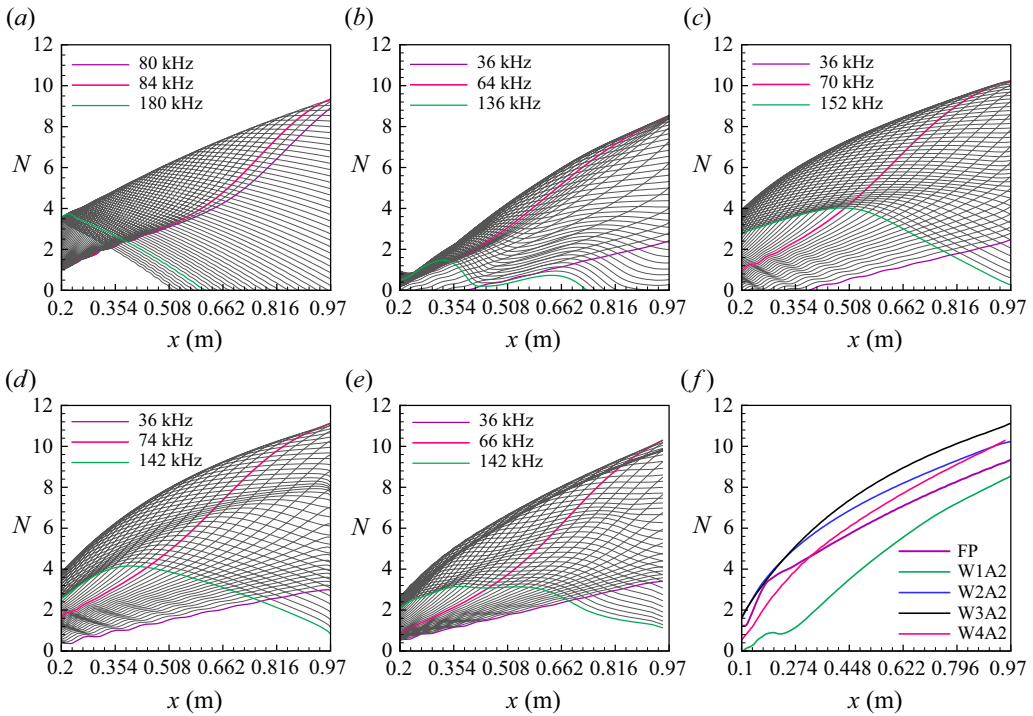
Figure 24. Effect of variation of roughness wavelength on the *N*-factor for a range of disturbance frequency plotted as a function of steamwise distance with a step of 2 kHz. The magenta line indicating the frequency leading to the maximum *N*-factor at the end of the domain corresponding to (*a*) smooth flat plate, (*b*) W1A2, (*c*) W2A2, (*d*) W3A2 and (*e*) W4A2. (*f*) The envelope of the maximum *N*-factor for each case.

(see figure 25*a*). The second-mode unstable region spans a frequency of 49−140 kHz. Mack's third mode is also noticed, which was not present for the smallest-roughness-height case shown in figure 15(*a*) for the range of frequencies considered. The magenta line in the figure indicates the averaged growth rate value computed over the roughness wavelength from the LST data.

As mentioned in § 4.3.6, the average growth rate variation is dominated by the second mode; however, lower frequencies are dictated by the first mode. A comparison of the averaged LST growth rate with the LDS data is shown in figure 25(*d*), where LST provides a good estimation of the unstable region, however, with a slightly lower second-mode peak growth rate. As the roughness wavelength is increased to $\lambda = 0.0016$ m, the first- and the second-mode-dominated regions extend to much larger frequencies (see figure 25*b*). Although the third mode is present, it becomes stable when averaged over the roughness wavelength. Compared with the LDS data, LST provides a significantly lower peak growth rate of the second mode that emerges at around 65 kHz in figure 25(*e*). For the second instability peak at 129 kHz, the amplification rate between LST and LDS is in close agreement. The second mode dominates the instability peak with the largest average growth rate, while the first mode also shows some amplification in this frequency range. The LST results suggest that the second local maximum in growth rate for W3A2 is also related to second-mode growth and not due to a different instability mechanism. For the W4A2 case, LST predicts a similar unstable region in frequency to that observed in LDS. The growth rate plot extracted from the LDS displays multiple peaks; however, as the peaks present until a frequency of 139 kHz lie inside the same neutral loop as predicted by
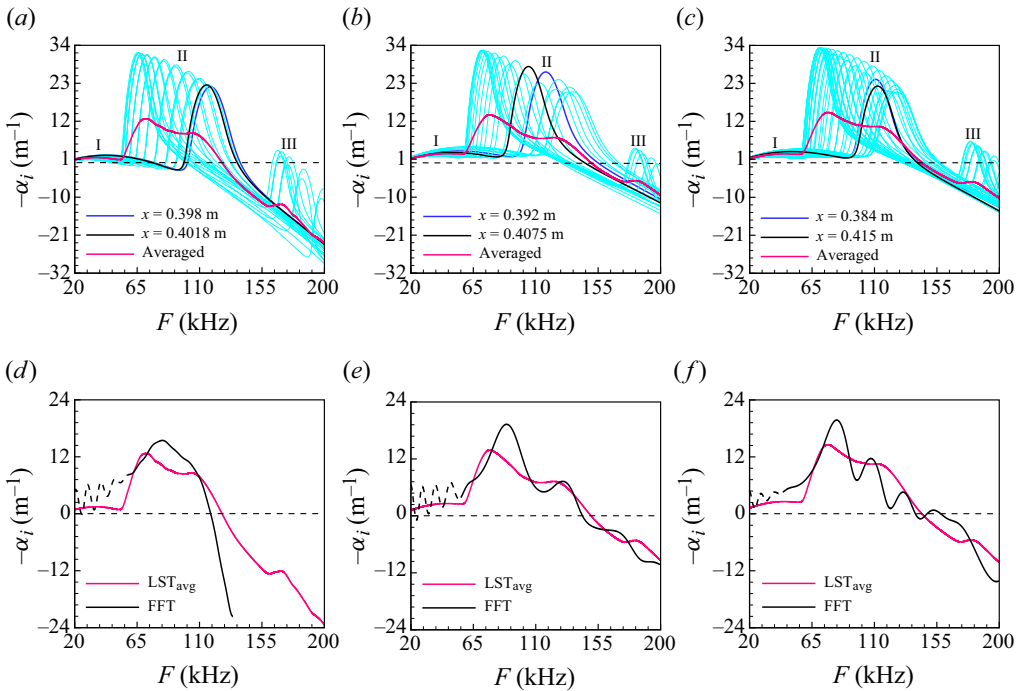
Figure 25. The variation of the LST growth rate along a roughness wavelength centred around $x = 0.4$ m, with the blue and the black lines denoting the first and the last location of the roughness element for cases (*a*) W1A2, (*b*) W3A2 and (*c*) W4A2. The magenta line corresponds to the averaged growth rate computed over the roughness wavelength obtained from the spatial LST solver, and (*d–f*) it is compared with the LDS growth rate.

LST, there is again only a single mode responsible for these peaks. Comparing the LDS and averaged LST growth rate variations, it can be affirmed that this mode is none other than the second mode. However, another small peak in growth rate at 152 kHz exists in the numerical data, which might be related to the third mode. This mode is stable according to LST and appears at a much larger frequency of around 180 kHz. Therefore, similar to the smooth flat plate and the amplitude-varying cases, the second mode is the dominant instability mechanism in the wavelength-varying cases, too. Also, there is no indication of a new instability mechanism generated due to surface roughness.

Finally, a comparison of the wavelength-varying cases is presented in figure 26. Similar to the LDS prediction in figure 26(*c*), LST shows a similar peak growth rate of the second mode for the three larger-wavelength cases at $x = 0.4$ m (figure 26*a*). The smallest-roughness-wavelength case leads to the lowest amplification of the first and the second modes, according to LST. The unstable region in frequency is also similar for the larger-wavelength cases. Case W1A2 shows a faster decay of the second mode, similar to what is observed in LDS. The frequency leading to maximum growth rate of the second mode is also slightly lower for W1A2 as compared with the other three rough-wall cases. Increasing the roughness wavelength increases the number of instability peaks, which shifts to a lower-frequency range, as observed from the numerical data in figure 26(*c*). Figure 26(*b,d*) presents the growth rate variation as a function of the non-dimensional frequency. This non-dimensional value is computed as $F_\lambda = F/(\bar{u}_e/\lambda)$, where λ is the
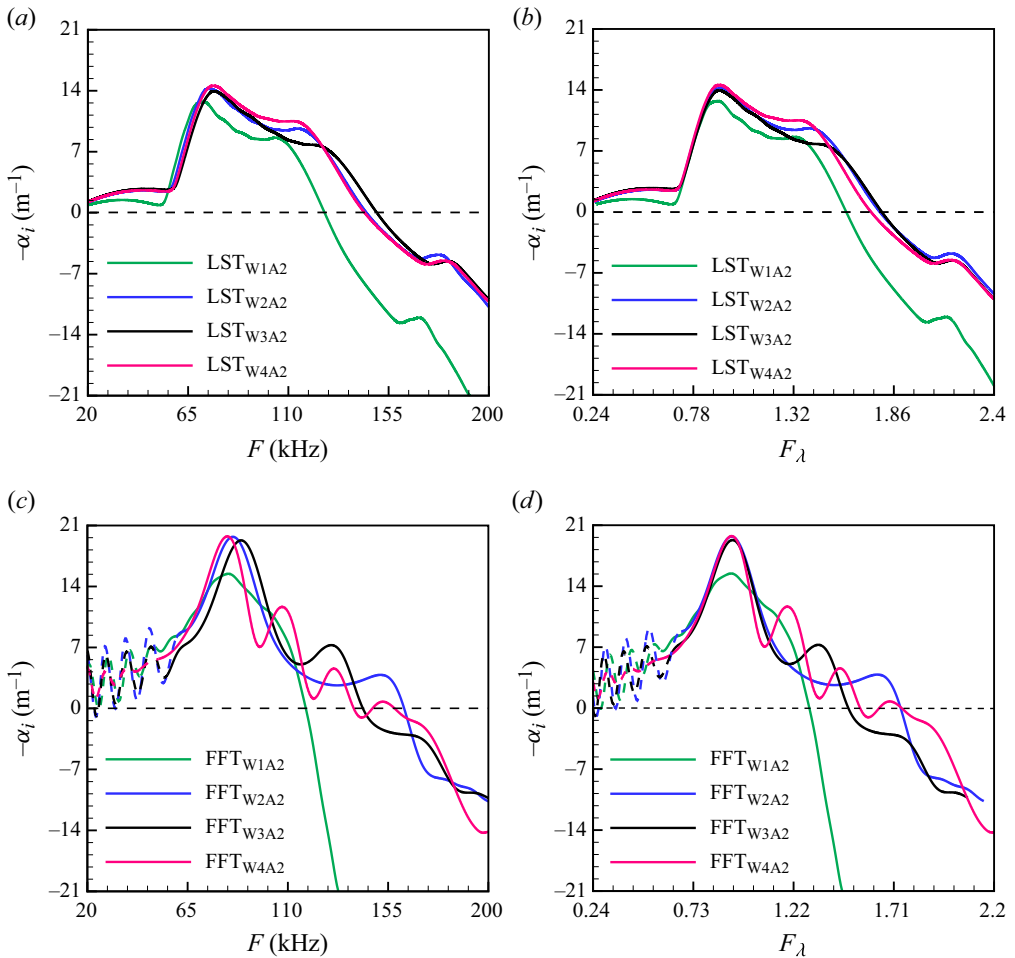
Figure 26. Effect of increasing the roughness wavelength on the averaged spatial growth rate over a roughness element centred at $x = 0.4$ m plotted as a function of disturbance frequency computed using (*a*) LST and (*c*) LDS. (*b,d*) The growth rate plotted as a non-dimensional frequency after normalising the frequency by the disturbance wavelength corresponding to the peak second-mode growth.

second-mode wavelength corresponding to its maximum amplification. Using this non-dimensional frequency, the dominant instability peaks in growth rate can be collapsed to a single frequency for all the wavelength-varying cases in both LST and LDS.

6. Conclusion

The stability characteristics of a hypersonic boundary-layer flow over smooth and rough walls were investigated using LDS and LST. The study was designed to isolate the effects of wavelength and height of parametrised sinusoidal surface roughness. Roughness amplitudes ranged from 10 % to 44 % of the boundary-layer height, and roughness wavelengths varied between 0.44 and 3.56 times the second-mode wavelength. Significant changes in mean flow were noted across all roughness scenarios, notably due to local flow separation and the generation of compression and expansion waves. Increasing the roughness height and the roughness wavelength enhances the strength of these wave patterns that interact with the disturbance flow field.

The disturbance flow fields near the wall resembled those over smooth walls, showing a typical two-cell structure for second-mode instabilities. Farther away from the wall, interactions between the second-mode-dominated wave packet and the mean-flow compression and expansion waves emanating from the rough surface induced acoustic-like disturbances in the free stream. In cases where the roughness wavelength is comparable to or exceeds the wavelength of the second mode, a consistent increase in the unstable region was observed as roughness heights were elevated, accompanied by the emergence of higher modes. The frequency range where the disturbances showed the largest amplification shifted to lower frequencies for all the rough-wall cases compared with the smooth-wall case. A comparison between the smooth flat plate and the case with the largest amplitude, designated as W2A4, demonstrated a notable reduction in the frequency corresponding to the peak N-factor, from 116 to 62 kHz.

However, a weak stabilisation of the flow to second-mode disturbances was observed for the shortest-roughness-wavelength case W1A2, which was included as part of the fixed-roughness-height cases. A comparative analysis of the wavy-wall cases W3A2 with W1A2 reveals that a reduction in wavelength by a factor of four leads to a decrease in the N-factor envelope from 11.2 to 8.54. A further reduction in the roughness wavelength from 44 % of the second-mode wavelength to 22 % results in a substantial decrease in the unstable frequency range. An analysis of the N-factor envelope reveals that the introduction of a minimal roughness height of 0.25 mm leads to a reduction in the N-factor compared with that of a smooth flat plate. Moreover, increasing the roughness height to 1 mm while maintaining the same roughness wavelength of 2 mm produces a significant stabilising effect, reducing the N-factor from 9.34 for the smooth-wall case to 3 for this configuration. Therefore, an increase in roughness height may exhibit either a stabilising or destabilising effect, depending on the relative size of the roughness wavelength in comparison with the wavelength of the second mode.

The amplitude plots obtained from the LDS displayed an interesting lobe structure hinting at altered instability mechanisms or a novel mechanism, possibly influenced by interactions with compression and expansion waves. LST was used to provide a detailed understanding of the stability characteristics of the flow. The LST analyses revealed rapid changes in stability characteristics along the roughness wavelength, with the lobed patterns in amplitude plots stemming from wavelength-averaged stability characteristics. These patterns reflect the combined influence of Mack's first, second and third modes rather than an unknown instability mechanism. A previously undiscovered instability mechanism could, therefore, be eliminated. The roughness heights considered in this study appear too small to cause the generation of dominant shear-layer instabilities. The frequency variation of the most amplified mode can be closely correlated to the change in boundary-layer thickness. The variation of the amplification rate followed the anticipated effects of adverse and favourable pressure gradients along the roughness wavelength. Although local LST cannot account for non-parallel effects, it aligns well with the LDS results, providing valuable insights into the flow's stability under varying surface roughness conditions.

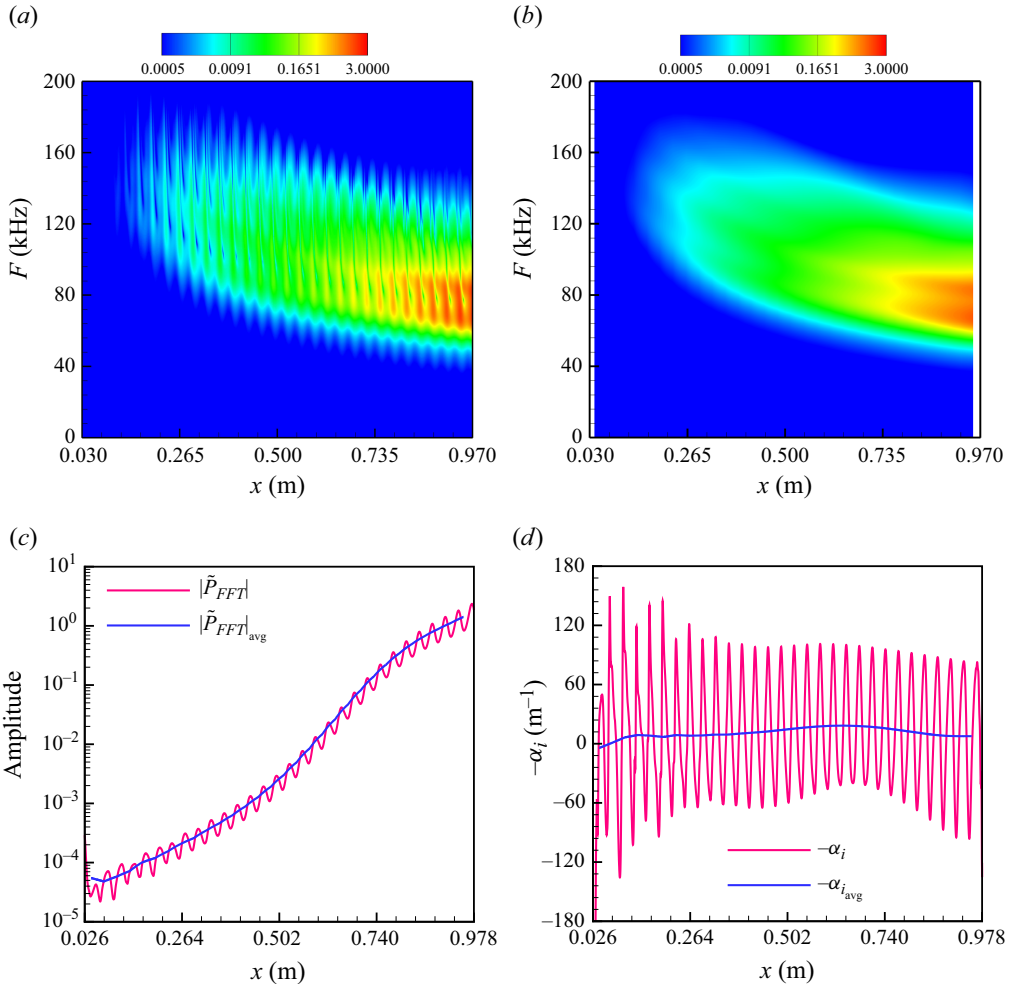**Declaration of interests.** The authors report no conflict of interest.

Figure 27. Fourier-transformed disturbance pressure amplitude for the rough-wall case W4A2 (*a*) before and (*b*) after averaging over each roughness wavelength. (*c*) Disturbance wall-pressure amplitude and (*d*) spatial growth rate extracted at $F = 68$ kHz, showing the actual and the roughness-averaged values along the surface.

Appendix A

Figure 27(*a*) plots the Fourier-transformed disturbance wall-pressure amplitude data for the rough-wall case W4A2 as a function of frequency. The non-smooth data indicate substantial variations due to the rough surface in the figure. After averaging over each roughness wavelength, the same data are presented in figure 27(*b*). The averaging process helps to eliminate the high oscillations present in the data. A comparison of the disturbance wall pressure and growth rate is shown in figures 27(*c*) and 27(*d*), respectively, after extracting at 68 kHz. When averaged over each roughness wavelength, wall pressure and growth data show a smooth variation along the plate.

Figures 28(*a*) and 28(*b*) plot the location along the plate where an *N*-factor of 8 is achieved for the amplitude-varying and wavelength-varying cases, respectively. The smooth-wall data are also included in both the figures for comparison with $A/A_{x=1\text{m}}$ (%) $= 0$ and $\lambda/\lambda_{2\text{nd}} = 0$. As the roughness amplitude increases, there is initially an upstream movement of the transition location. The flow is slightly stabilised as the
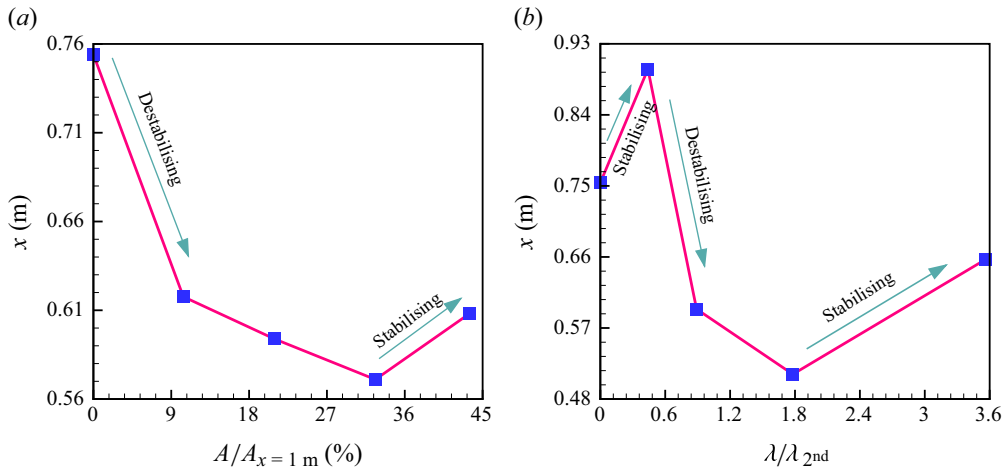
1008 A52-36

Figure 28. The streamwise location where an *N*-factor of 8 is reached plotted as a function of roughness (*a*) amplitude and (*b*) wavelength for the rough-wall cases presented in tables 1 and 2, respectively.

roughness height exceeds 33 % of the smooth-wall boundary-layer height. However, the transition location is still well ahead of that of the smooth flat plate case. For the wavelength-varying cases from table 2, the smallest-roughness-wavelength case leads to a downstream movement of the transition location from 0.75 m corresponding to the smooth-wall case to 0.9 m for the W1A2 case (see figure 28*b*). Compared with the smooth flat plate, all the larger-wavelength cases show an upstream movement of the transition location similar to the larger-amplitude-roughness cases in figure 28(*a*). As the roughness wavelength exceeds 1.8 times the second-mode wavelength corresponding to the smooth-wall case, there is again a significant downstream movement of the transition location; however, it is again well upstream of the smooth flat plate location.

Appendix B

Figure 29 illustrates the impact of a larger roughness wavelength ($\lambda = 16$ mm) with varying roughness heights on the Fourier-transformed disturbance pressure amplitude across a range of frequencies. The height of the distributed roughness elements has been systematically varied from 0.5 to 2 mm in 0.5 mm increments. An observed phenomenon is that as the amplitude of the roughness elements increases, the unstable region expands over a wider frequency spectrum. Particularly, in close proximity to the initial roughness location, the unstable region encompasses frequencies from a notably low level up to approximately 200 kHz at larger roughness heights.

The effect of roughness height at a smaller roughness wavelength of 2 mm is depicted in figure 30. In contrast to the scenario with a larger roughness wavelength, an increase in roughness height at a smaller wavelength results in a significant reduction of the unstable region in frequency. Elevating the height of the elements from 0.25 to 0.5 mm leads to a modest rise in disturbance amplitude, as indicated by the emergence of red contours in figure 30(*b*). However, a further increase in the roughness height to 1 mm causes a decrease in disturbance growth as well as the unstable region in frequency.

A comparison of the *N*-factor envelope with the smooth-wall data for both large- and small-roughness-wavelength cases is presented in figure 31. It is evident from figure 31(*a*) that the introduction of roughness elements, regardless of their height, leads to an increase in the *N*-factor when compared with the smooth flat plate at a large roughness wavelength
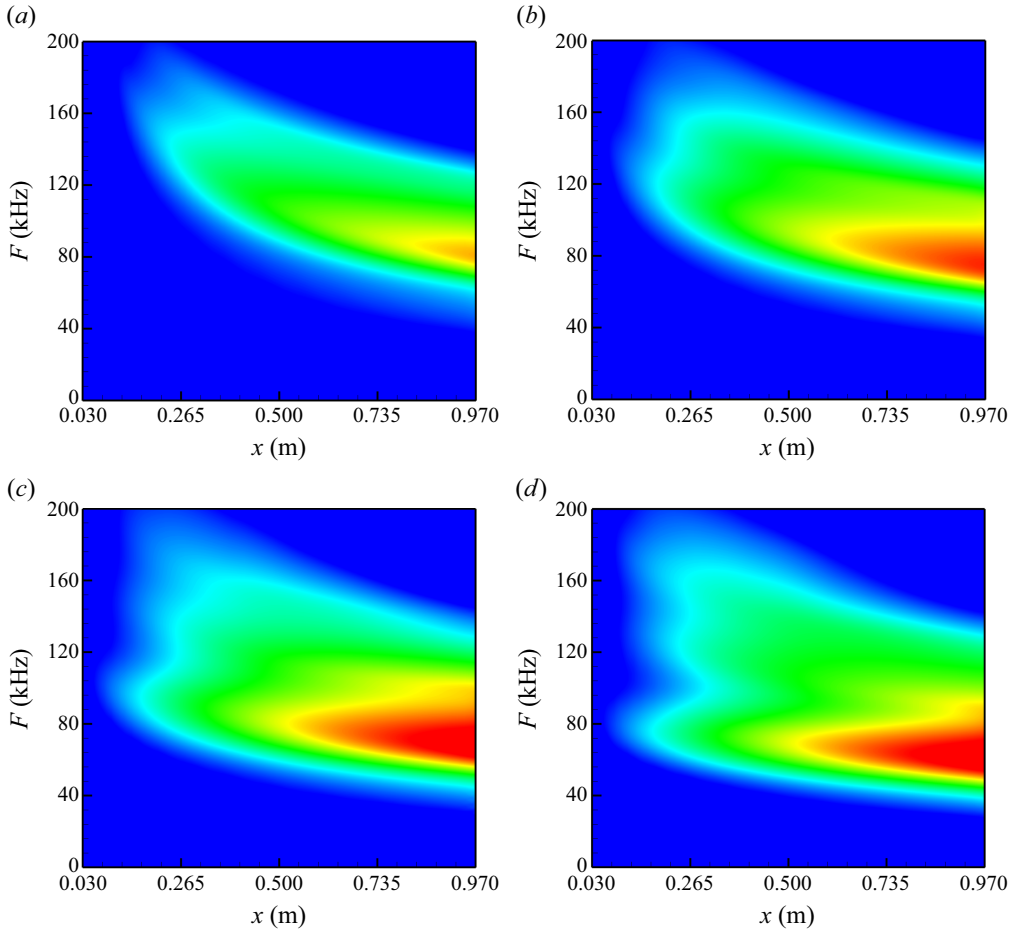
Figure 29. Contours of Fourier-transformed disturbance pressure amplitude as a function of frequency and streamwise location for the wavy-wall case with a wavelength of 16 mm and a roughness height of (*a*) 0.5 mm, (*b*) 1 mm, (*c*) 1.5 mm and (*d*) 2 mm.
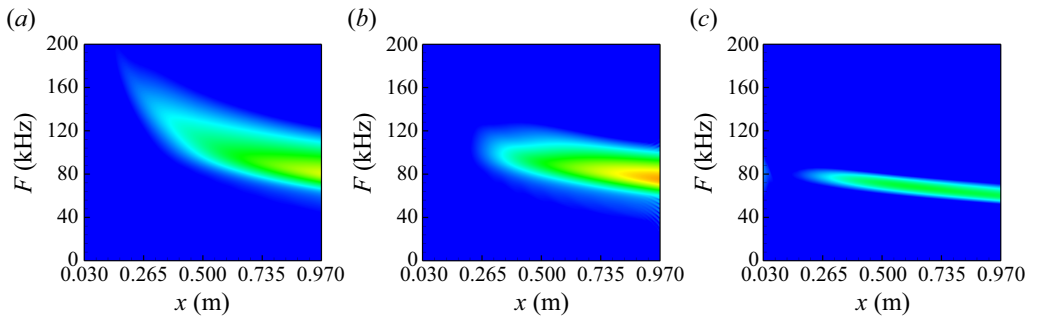

Figure 30. Contours of Fourier-transformed disturbance pressure amplitude as a function of frequency and streamwise location for the wavy-wall case with a wavelength of 2 mm and a roughness height of (*a*) 0.25 mm, (*b*) 0.5 mm and (*c*) 1 mm.
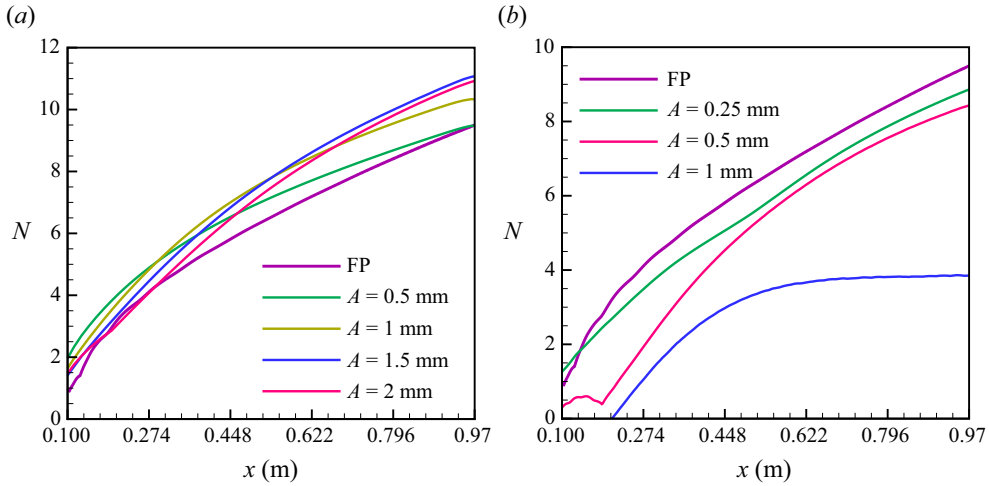
(a)

(b)

Figure 31. Effect of variation of roughness height on the *N*-factor envelope for the wavy-wall case with a wavelength of (*a*) 16 mm and (*b*) 2 mm.
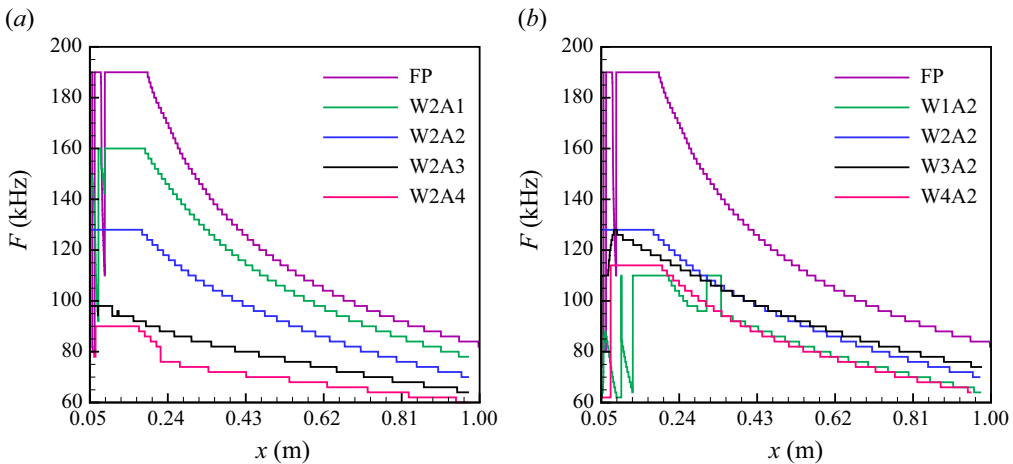
(a)

(b)

Figure 32. The frequency leading to the maximum *N*-factor envelope for the (*a*) amplitude-varying cases and (*b*) wavelength-varying cases.

of 16 mm. However, the influence of roughness is more pronounced at a smaller roughness height of 2 mm. The introduction of a small roughness height of 0.25 mm results in a decrease in the *N*-factor when compared with the case of a smooth flat plate. Moreover, the presence of distributed roughness elements with a roughness height of 1 mm demonstrates a notable stabilising effect, yielding an *N*-factor of approximately 3 downstream of $x = 0.45$ m, which continues throughout the rest of the domain.

Appendix C

For a detailed comparison between the smooth-wall and wavy-wall cases, we computed the frequencies associated with the maximum *N*-factor at each streamwise location for both configurations. It is evident that as the boundary-layer thickness increases along the plate, there is a corresponding reduction in frequency linked to the most unstable mode, as demonstrated in figure 32. Furthermore, an increase in the amplitude of roughness yields a

similar decrease in disturbance frequency, which can be attributed to a rise in the effective boundary-layer height (as illustrated in figure 32*a*). Conversely, in cases with varying wavelengths, although there is a significant drop in the frequency of the smooth wall, only minor changes in the frequency associated with the maximum *N*-factor are observed among the wavy-wall cases.

REFERENCES

BERRY, S.A., AUSLENDER, A.H., DILLEY, A.D. & CALLEJA, J.F. 2001 Hypersonic boundary-layer trip development for hyper-x. *J. Spacecr. Rockets* **38** (6), 853–864.

BORG, M.P., ADAMCZAK, D.W., CULLER, A.J. & KURTZ, M.D. 2025 Hiflier hypersonic flight experiment: Design, analysis, and ground test. In *AIAA SCITECH. 2025 Forum*, pp. 0733. American Institute of Aeronautics and Astronautics.

BOUNTIN, D., CHIMITOV, T., MASLOV, A., NOVIKOV, A., EGOROV, I., FEDOROV, A. & UTYUZHNIKOV, S. 2013 Stabilization of a hypersonic boundary layer using a wavy surface. *AIAA J.* **51** (5), 1203–1210.

BRAGA, M., DUNGAN, S. & BREHM, C. 2024*a* Numerical investigation of laminar-turbulent transition for hypersonic blunt bodies with distributed roughness. *Bull. Am. Phys. Soc.* APS Divison of Fluid Dynamics Meeting Abstracts, A27–003.

BRAGA, M.A., DUNGAN, S., BREHM, C. & MACDONALD, R.L. 2024b Numerical simulation of boundary layer transition on mach 6 cylinder with randomly phased sinusoidal roughness. In *AIAA SCITECH. 2024 Forum*, 1976. American Institute of Aeronautics and Astronautics.

BREHM, C., BARAD, M.F., HOUSMAN, J.A. & KIRIS, C.C. 2015 A comparison of higher-order finite-difference shock capturing schemes. *Comput. Fluids* **122**, 184–208.

BREHM, C., DACKERMANN, T., GRYGIER, F. & FASEL, H. 2011 Numerical investigations of the influence of distributed roughness on Blasius boundary layer stability. In *49th AIAA Aerospace Sciences Meeting including the New Horizons Forum and Aerospace Exposition*, pp. 563. American Institute of Aeronautics and Astronautics.

BREHM, C. & FASEL, H. F. 2013 A novel concept for the design of immersed interface methods. *J. Comput. Phys.* **242**, 234–267.

BROWNE, O.M., HAAS, A.P., FASEL, H.F. & BREHM, C. 2019 An efficient linear wavepacket tracking method for hypersonic boundary-layer stability prediction. *J. Comput. Phys.* **380**, 243–268.

BROWNE, O.M., HAAS, A.P., FASEL, H.F. & BREHM, C. 2020 A nonlinear wavepacket tracking method for hypersonic boundary-layer flows on irregular domains. In *AIAA Aviation 2020 Forum*, 2985. American Institute of Aeronautics and Astronautics.

BROWNE, O.M., HAAS, A.P., FASEL, H.F. & BREHM, C. 2022 A nonlinear compressible flow disturbance formulation for adaptive mesh refinement wavepacket tracking in hypersonic boundary-layer flows. *Comput. Fluids* **240**, 105395.

BUCCI, M.A., PUCKERT, D.K., ANDRIANO, C., LOISEAU, J.-C., CHERUBINI, S., ROBINET, J.-C. & RIST, U. 2018 Roughness-induced transition by quasi-resonance of a varicose global mode. *J. Fluid Mech.* **836**, 167–191.

CHOUDHARI, M.M., LI, F. & PAREDES, P. 2018 Effect of distributed patch of smooth roughness elements on transition in a high-speed boundary layer. In *2018 Fluid Dynamics Conference*, pp. 3532. American Institute of Aeronautics and Astronautics.

DI GIOVANNI, A. & C., STEMMER 2018 Direct numerical simulations of roughness-induced transition in the boundary layer of a hypersonic spherical forebody under consideration of high-temperature gas effects. In *2018 Fluid Dynamics Conference*, pp. 4046. American Institute of Aeronautics and Astronautics.

DI GIOVANNI, A. & STEMMER, C. 2019 Roughness-induced boundary-layer transition on a hypersonic capsule-like forebody including nonequilibrium. *J. Spacecr. Rockets* **56** (6), 1795–1808.

DONG, M. & ZHAO, L. 2021 An asymptotic theory of the roughness impact on inviscid mack modes in supersonic/hypersonic boundary layers. *J. Fluid Mech.* **913**, A22.

DUAN, L., WANG, X. & ZHONG, X. 2010 A high-order cut-cell method for numerical simulation of hypersonic boundary-layer instability with surface roughness. *J. Comput. Phys.* **229** (19), 7207–7237.

FEDOROV, A. & TUMIN, A. 2011 High-speed boundary-layer instability: old terminology and a new framework. *Aiaa J.* **49** (8), 1647–1657.

FLORYAN, J. 1997 Stability of wall-bounded shear layers in the presence of simulated distributed surface roughness. *J. Fluid Mech.* **335**, 29–55.

FONG, K.D., WANG, X. & ZHONG, X. 2014 Numerical simulation of roughness effect on the stability of a hypersonic boundary layer. *Comput. Fluids* **96**, 350–367.

HAAS, A.P., BROWNE, O.M., FASEL, H.F. & BREHM, C. 2020 A time-spectral approximate Jacobian based linearized compressible Navier–Stokes solver for high-speed boundary-layer receptivity and stability. *J. Comput. Phys.* **405**, 108978.

HOLLIS, B.R. 2021 Hexcomb-pattern roughness effects on blunt-body transition and heating. *J. Spacecr. Rockets* **58** (6), 1612–1635.

IYER, P., MUPPIDI, S. & MAHESH, K. 2011 Roughness-induced transition in high speed flows. In *49th AIAA Aerospace Sciences Meeting including the New Horizons Forum and Aerospace Exposition*, pp. 566. American Institute of Aeronautics and Astronautics.

IYER, P., MUPPIDI, S. & MAHESH, K. 2012 Boundary layer transition in high-speed flows due to roughness. In *50th AIAA Aerospace Sciences Meeting including the New Horizons Forum and Aerospace Exposition*, pp. 1106. American Institute of Aeronautics and Astronautics.

KHOTYANOVSKY, D., KIRILOVSKIY, S., POPLAVSKAYA, T. & KUDRYAVTSEV, A. 2019 Numerical study of the evolution of disturbances generated by roughness elements in a supersonic boundary layer on a blunted cone. *J. Appl. Mech. Tech. Phys.* **60** (3), 438–450.

LOISEAU, J.-C., ROBINET, J.-C., CHERUBINI, S. & LERICHE, E. 2014 Investigation of the roughness-induced transition: global stability analyses and direct numerical simulations. *J. Fluid Mech.* **760**, 175–211.

MA, R. & MAHESH, K. 2022 Global stability analysis and direct numerical simulation of boundary layers with an isolated roughness element. *J. Fluid Mech.* **949**, A12.

MACK, L.M. 1975 Linear stability theory and the problem of supersonic boundary-layer transition. *Aiaa J.* **13** (3), 278–289.

MACK, L.M. 1984 Boundary-layer linear stability theory. Tech. Rep. California Inst of Tech Pasadena Jet Propulsion Lab.

MACK, L.M. 1987 Review of linear compressible stability theory. In *Stability of Time Dependent and Spatially Varying Flows*, pp. 164–187. Springer.

MUPPIDI, S. & MAHESH, K. 2012 Direct numerical simulations of roughness-induced transition in supersonic boundary layers. *J. Fluid Mech.* **693**, 28–56.

PAREDES, P., CHOUDHARI, M., CARPENTER, M.H. & LI, F. 2024 The harmonic linearized Navier–Stokes equations for transition prediction in three-dimensional flows. *Comput. Fluids* **273**, 106206.

SAIKIA, B. & BREHM, C. 2022 Effects of distributed surface roughness on supersonic boundary layer receptivity mechanisms. In *AIAA AVIATION. 2022 Forum*, pp. 4101. American Institute of Aeronautics and Astronautics.

SAIKIA, B. & BREHM, C. 2024 Effects of injection gas composition on the stability of a high-enthalpy flow over a blunt cone. In *AIAA SCITECH. 2024 Forum*, pp. 1977. American Institute of Aeronautics and Astronautics.

SCHNEIDER, S.P. 2008*a* Effects of roughness on hypersonic boundary-layer transition. *J. Spacecr. Rockets* **45** (2), 193–209.

SCHNEIDER, S.P. 2008*b* Summary of hypersonic boundary-layer transition experiments on blunt bodies with roughness. *J. Spacecr. Rockets* **45** (6), 1090–1105.

SCHNEIDER, S.P. 2010 Hypersonic boundary-layer transition with ablation and blowing. *J. Spacecr. Rockets* **47** (2), 225–237.

SEMPER, M.T. & BOWERSOX, R.D. 2017 Tripping of a hypersonic low-Reynolds-number boundary layer. *Aiaa J.* **55** (3), 808–817.

SHRESTHA, P. & CANDLER, G.V. 2019 Direct numerical simulation of high-speed transition due to roughness elements. *J. Fluid Mech.* **868**, 762–788.

SI, W., HUANG, G., ZHU, Y., CHEN, S. & LEE, C. 2019 Hypersonic aerodynamic heating over a flared cone with wavy wall. *Phys. Fluids* **31** (5), 051702.

SIVASUBRAMANIAN, J. & FASEL, H. 2011 Transition initiated by a localized disturbance in a hypersonic flat-plate boundary layer. In *49th AIAA Aerospace Sciences Meeting including the New Horizons Forum and Aerospace Exposition*, pp. 374. American Institute of Aeronautics and Astronautics.

TUMIN, A. 2006 Three-dimensional spatial normal modes in compressible boundary layers. In *44th AIAA Aerospace Sciences Meeting and Exhibit*, pp. 1109. American Institute of Aeronautics and Astronautics.

TUMIN, A. 2007 Three-dimensional spatial normal modes in compressible boundary layers. *J. Fluid Mech.* **586**, 295–322.

TUMIN, A. 2008 Nonparallel flow effects on roughness-induced perturbations in boundary layers. *J. Spacecr. Rockets* **45** (6), 1176–1184.

ZHAO, L., DONG, M. & YANG, Y. 2019 Harmonic linearized Navier–Stokes equation on describing the effect of surface roughness on hypersonic boundary-layer transition. *Phys. Fluids* **31** (3), 034108.

ZHOU, Y., LIU, W., CHAI, Z. & YANG, X. 2017 Numerical simulation of wavy surface effect on the stability of a hypersonic boundary layer. *Acta Astronaut.* **140**, 485–496.

ZOPPINI, G., WESTERBEEK, S., RAGNI, D. & KOTSONIS, M. 2022 Receptivity of crossflow instability to discrete roughness amplitude and location. *J. Fluid Mech.* **939**, A33.